Revision 4_Manuscript 5838

Tourmaline-rich features in the Heemskirk and Pieman Heads granites from western Tasmania, Australia: Characteristics, origins, and implications for tin mineralization

Wei Hong[1, *], David R. Cooke[1, 2], Lejun Zhang[1, 2], Nathan Fox[1], and Jay Thompson[1]

[1] ARC Centre of Excellence in Ore Deposits (CODES), University of Tasmania, Private Bag 79, Hobart 7001, Australia

[2] Transforming the Mining Value Chain, an ARC Industrial Transformation Research Hub, University of Tasmania, Private Bag 79, Hobart 7001, Australia

[*] Corresponding author: E-mail, wei.hong@utas.edu.au

Abstract

Distinctive magmatic-hydrothermal tourmaline-rich features have developed in the Heemskirk and Pieman Heads granites from western Tasmania, Australia. They are categorized as tourmaline-rich patches, orbicules, cavities, and veins, based on their distinctive morphologies, sizes, mineral assemblages, and contact relationships with host granites. These textural features occur in discrete layers in the roof zone of granitic sills within the Heemskirk and Pieman Heads granites. Tourmaline patches commonly occur below a tourmaline orbicule-rich granitic sill. Tourmaline-filled cavities have typically developed above the tourmaline-quartz orbicules in the upper layer of the white phase of the Heemskirk Granite. Tourmaline-quartz veins penetrate all exposed levels of the granites, locally cutting tourmaline orbicules and cavities.

The tourmalines are mostly schorl (Fe-rich) and foitite, with an average end-member component of schorl$_{45}$ dravite$_{6}$ tsilaisite$_{1}$ uvite$_{0}$ Fe-uvite$_{3}$ foitite$_{31}$ Mg-foitite$_{4}$ olenite$_{10}$. Element substitutions of the tourmalines are controlled by $FeMg_{-1}$, $^{Y}Al^{X}\square(R^{2+}Na)_{-1}$, and minor $^{Y}AlO(R^{2+}OH)_{-1}$ (where $R^{2+} = Fe^{2+} + Mg^{2+} + Mn^{2+}$) exchange vectors. A number of trace elements in tourmaline have consistent chemical evolutions grouped from tourmaline patches, through orbicules and cavities, to veins. There

is a progressive decrease of most transition and large ion lithophile elements, and a gradual increase of most high field strength elements. These compositional variations in the different tourmaline-rich features probably relate to element partitioning occurring in these phases due to volatile exsolution and fluxing of aqueous boron-rich fluids that separated from the granitic melts during the emplacement of S-type magmas into the shallow crust (4 to 5.5 km).

Tourmalines from the Heemskirk Granite are enriched in Fe, Na, Li, Be, Sn, Ta, Nb, Zr, Hf, Th, and rare earth elements relative to the tourmalines from the Pieman Heads Granite, but depleted in Mg, Mn, Sc, V, Co, Ni, Pb, Sr, and most transition elements. These results imply that bulk compositions of the host granites exert a major control on the chemical variations of tourmalines. The trace element compositions of tourmalines from the Sn-mineralized Heemskirk Granite are different from those of the barren Pieman Heads Granite. Trace element ratios (e.g., Zn/Nb, Co/Nb, Sr/Ta, and Co/La) and Sn concentrations in tourmaline can distinguish the productive Heemskirk Granite from the barren Pieman Heads Granite.

Keywords: tourmaline, orbicules, mineral chemistry, granites, Tasmania

INTRODUCTION

Tourmaline orbicules are distinctive textures that mostly occur in leucocratic granites which have formed across a broad spectrum of time and space. They have been found in the Paleoproterozoic Scruber granite, Western Australia (Shewfelt 2005); the Neoproterozoic Cape Granite Suite, South Africa (Rozendaal and Bruwer 1995); the Carboniferous to Permian Bohemian Massif, Czech Republic (Buriánek and Novák 2007); the Cretaceous Seagull Batholith, Yukon Territory, Canada (Sinclair and Richardson 1992); the late Miocene Capo Bianco aplite, Elba Island, Italy (Perugini and Poli 2007), and many other locations, including the peraluminous leucogranites at Cornwall, southwest England (London and Manning 1995; Drivenes et al. 2015). Tourmaline orbicules have been known by a variety of names, including tourmaline nodules, spots, clots, ovoids, and clusters. They are typically 8-10 cm in diameter, rounded to sub-rounded, and consist of

tourmaline, quartz, and minor feldspar, muscovite, and trace amounts of monazite, zircon, apatite, titanite, and other accessory phases.

Although features of tourmaline orbicules are well-documented, their origins have been hotly debated. Two contrasting hypotheses have been proposed for their origins: (1) post-magmatic metasomatism by boron-rich hydrothermal fluids from adjacent crystallizing granites (Dick 1980; Le Fort 1991; Rozendaal and Bruwer 1995), or (2) deposition from hydrous boron-rich fluids that unmixed from granitic melts (Sinclair and Richardson 1992; Samson and Sinclair 1992; Jiang et al. 2003; Shewfelt 2005; Buriánek and Novák 2007; Dini et al. 2007; Perugini and Poli 2007; Trumbull et al. 2008; Balen and Broska 2011; Drivenes et al. 2015). Tourmaline orbicules potentially have exploration significance, because they occur in some felsic granites that are genetically associated with Sn-W deposits (e.g., Hajitaheri 1985; Sinclair and Richardson 1992; Samson and Sinclair 1992; Rozendaal and Bruwer 1995; London and Manning 1995; Drivenes et al. 2015).

Tourmaline can display distinctive optical, chemical, and isotopic growth zonation patterns that record the geological conditions under which they precipitate (van Hinsberg et al. 2011a). Tourmaline is exceptionally refractory, and can preserve its compositions during physical and chemical changes associated with sedimentary, metamorphic, and igneous processes (Henry and Guidotti 1985), due to low element diffusion rates in its crystal structure (van Hinsberg et al. 2011a, 2011b). These characteristics potentially make tourmaline a petrological ‘forensic’ mineral (van Hinsberg et al. 2011a).

Despite its widespread occurrence in diverse geological environments, there have been only a few studies of trace element systematics of tourmaline (e.g., Griffin at al. 1996; Jiang et al. 2004; Yavuz et al. 2011). Laser ablation inductively coupled plasma mass spectrometry (LA-ICP-MS) has recently been applied to determine trace element concentrations of tourmaline from diverse environments (van Hinsberg 2011; Marks et al. 2013; Roda-Robles et al. 2015; Drivenes et al. 2015). Compared to traditional electron microprobe analysis of minerals, in-situ LA-ICP-MS technique

shows great advantages in detecting trace element concentration anomalies that have potential importance for mineralization and exploration (e.g., Cooke et al. 2014; Wilkinson et al. 2015).

The purpose of this study is to document tourmaline orbicules and other tourmaline-rich magmatic – hydrothermal assemblages (i.e., tourmaline patches, cavities, and veins) developed in the Heemskirk and Pieman Heads granites from western Tasmania, Australia. The origins of these tourmaline-rich features are investigated using LA-ICP-MS in order to determine trace element systematics in tourmaline from different features, in combination with bulk-rock and electron microprobe analyses. The potential of tourmaline mineral chemistry as a fertility indicator in distinguishing Sn-mineralized from barren host-granites is assessed.

GEOLOGICAL BACKGROUND

Regional geological evolution

The western Tasmanian terrain has undergone a relatively complex geological evolution. It consists of a variety of sedimentary sequences, ranging from Mesoproterozoic to Quaternary, which crop out across the western two-thirds of Tasmania (Fig. 1; Seymour et al. 2007). The Proterozoic basements in western Tasmania consist of the Meso- to Neoproterozoic Rocky Cape Group (Halpin et al. 2014) in the northwest, and the Tyennan metasedimentary rocks in the central-west, as well as the Neoproterozoic Oonah Formation (Fig. 1). Another cycle of sedimentation on the passive continental margin produced the Neoproterozoic Togari Group, which accumulated until the Early Cambrian (ca. 520 Ma; Seymour et al. 2007).

An arc-continent collision from the early to middle Cambrian characterized the Cambrian Tyennan Orogeny (Berry and Crawford 1988), and generated the Mt Read volcanic rocks (Fig. 1) which host the most economically important volcanic-hosted massive sulfide deposits in Australia (Large 1992). Late Cambrian basin inversion resulted in major reverse faulting and uplifting of the Tyennan region, which shed voluminous coarse siliciclastic conglomerates (Owen Group) into

half-grabens (Seymour et al. 2007). Ordovician to Early Silurian shallow marine sedimentary rocks (Gordon Group) unconformably overlie the Owen Group sequences. The Gordon Group units are overlain unconformably by thick marine siliciclastic sediments of the Silurian to Early Devonian Eldon Group (Seymour et al. 2007). NNW-oriented fold and fault systems throughout Tasmania formed during the Devonian Tabberabberan Orogeny (Seymour et al. 2007).

Extensive felsic magmatism affected eastern and western Tasmania during the Devonian to Early Carboniferous, younging progressively westward (Black et al. 2005). Large volumes of granitoid batholiths intruded the eastern Tasmanian terrain (McClenaghan 2006), showing a geochemical trend from old mafic unfractionated granodiorites (ca. 400 Ma), through felsic, weakly fractionated I- and S-type monzogranites (390 – 387 Ma) towards young felsic, highly fractionated I- and S-type leucogranites (ca. 378 Ma). In contrast, scattered western Tasmanian granites have relatively small exposures (Fig. 1). They are dominated by fractionated felsic I- and S-type granites that intruded between 373 and 350 Ma (Black et al. 2005). At least three of the western Tasmanian granites (the Pine Hill, Meredith, and Heemskirk plutons) are associated with world-class Sn-W deposits (Fig. 1; Solomon and Groves 2000; Green 2012; Table 1).

Heemskirk and Pieman Heads granites

The Heemskirk Batholith is exposed over 140 km^2 on the western coastline of Tasmania (Fig. 1). The batholith intruded the Neoproterozoic Oonah Formation to the north and east (Fig. 2). On its southern edge, the Heemskirk Batholith has sub-vertical intrusive contacts with the Oonah metasedimentary rocks, and has also intruded Cambrian volcanics, gabbro, serpentinized dunite, and Silurian – Devonian sedimentary rocks (Fig. 2a). The granite contains two main phases, the white and the red phases (Fig. 2a). This classification is mainly based on the distinctive color of orthoclase feldspar in both units (Klominsky 1972). Both the white and red granites principally consist of quartz, K-feldspar, plagioclase, and minor biotite or muscovite. Accessory minerals such as zircon, monazite,

ilmenite, and apatite occur in both granite phases. Hornblende, allanite, titantite, magnetite are typically observed in the red granite, whereas muscovite, garnet and cassiterite only occur in the white granite (Klominsky, 1972; Hajitaheri, 1985). Tourmaline occurs in both granite phases, but is more abundant in the white granite. The red granite overlies the white granite (Fig. 2b). Precise SHRIMP zircon U-Pb dating cannot distinguish the red granite (360 ± 2 Ma) from the white granite (361 ± 2 Ma; Black et al. 2005). The granitic batholith extends beneath the Zeehan and Dundas fields, and gravity modeling shows that it may connect with the Pine Hill and Granite Tor granites at depth > 2 km (Leaman and Richardson 2003; Fig. 1). Hajitaheri (1985) estimated a minimum crystallization temperature of 700 °C and pressure of 1kbar for the Heemskirk Granite, based on mineral thermometry. An oxidation state between magnetite-hematite and Ni-NiO buffer was suggested to the original magmas of the red phase of the Heemskirk Granite, whereas the oxidation state of the white Heemskirk Granite lies below the Ni-NiO buffer (Hajitaheri, 1985).

The Heemskirk Granite is a fertile intrusion, because it is genetically and spatially associated with abundant Sn-W skarn, greisen deposits, and vein-type Ag-Pb-Zn deposits (Figs. 1 and 2a; Table 1). More than 35 ore occurrences have been historically mined from the Heemskirk Granite since 1876 (Waterhouse 1916; Purvis 1989). The largest Sn-W deposits include Federation, Globe, Sweeneys, Colemans, Tenth Legion, and St Dizier (Table 1). These Sn-W skarns and greisens are estimated to contain at least 0.03 Mt of tin (Purvis 1989; Seymour et al. 2007; Table 1). The highly unusual Avebury deposit contains a resource of 29.3 Mt at 0.9 % nickel. The hydrothermal nickel deposit formed at the contact between the southern edge of the Heemskirk Granite and ultramafic-mafic rocks (Keays and Jowitt 2013; Table 1).

Other significant Sn-W skarn deposits, such as the Severn, Queen Hill, Montana and Oonah, have been discovered in the Zeehan field, overlying the subsurface eastern flank of the Heemskirk Granite (Leaman and Richardson 2003; Fig 1). These Sn-W skarns contain > 0.104 Mt of tin (Purvis 1989; Seymour et al. 2007; Callaghan 2013 unpublished; Table 1). More than 0.19 Mt of lead and

750 t of silver were mined in the Zeehan field from the 1880s to 1950s (Both and Williams 1968; Fig 1). The substantial zinc contents of the ores could not be recovered by the processing techniques available at that time.

No mineralization has been discovered in or around the Pieman Heads Granite. This intrusion is located 20 km north of the white phase of the Heemskirk Granite, and has a much smaller surface exposure (ca. 8 km^2; Fig. 1). The granite intruded the Neoproterzoic Rocky Cape Group, a sequence of metamorphic slates, quartzites, and dolomites. The granite is partly overlain by Tertiary and Quaternary sedimentary rocks (Fig. 1). The Pieman Heads Granite contains quartz, K-feldspar, plagioclase, biotite, and minor muscovite, with accessory tourmaline, apatite, zircon, monazite, and titanite. It has a LA-ICP-MS zircon U-Pb age of 365.5 ± 4 Ma (Hong et al. submitted manuscript), overlapping in analytical error with the Heemskirk Granite (Black et al. 2005). The Pieman Heads and NNW-elongate Interview River granites are situated on the southern and northern sides of the Pieman River mouth, respectively (Fig. 1). These two plutons, together with the Sandy Cape and Three Hummock Island granites, have been grouped as the 'Sandy Cape Suite' (Sawka et al. 1990). Geophysical investigations have shown that the Pieman Heads Granite is probably connected with the Interview River Granite and the Sandy Cape Granite at depths below 1 km (Leaman and Richardson 2003).

TOURMALINE- AND QUARTZ-RICH FEATURES

Tourmaline nodules in the Heemskirk Batholith were described by Klominsky (1972) and Hajitaheri (1985). The contacts between the white and red phases of this granite, and the contacts of the white granite with local country rocks, have developed abundant magmatic – hydrothermal features dominated by quartz and tourmaline (Fig. 2). In the current study, these features are divided into (1) tourmaline patches, (2) tourmaline-quartz orbicules, (3) tourmaline-filled cavities, and (4) tourmaline-quartz veins, largely according to their morphologies, sizes, mineral assemblages, and

contact relationships with their host granites (Table 2; Fig. 2c). Quartz-rich unidirectional solidification textures (USTs, cf. Shannon et al. 1982) are also exposed in the upper part of the white phase of the Heemskirk Granite, and have a close spatial association with the tourmaline orbicules.

Within the Sandy Cape Suite, the Pieman Heads Granite is exceptional for its distinctive tourmaline nodules (Sawka et al. 1990). These magmatic – hydrothermal features are similar to those that occur within the Heemskirk Batholith. Tourmaline patches, orbicules, and tourmaline-quartz veins have been classified in the upper portion of the Pieman Heads Granite (Table 2). Tourmaline-filled miarolitic textures and USTs have not been observed in the Pieman Heads Granite.

Tourmaline patches

Tourmaline patches are typically disseminated at lower levels within the Heemskirk (Fig. 2c) and Pieman Heads granites. They are commonly 0.5-3 cm in diameter, and exhibit irregular and dendritic morphologies (Fig. 3a; Table 2). Tourmaline patches have been observed in both the red and white phases of Heemskirk Granite, but are more common in lower layers of the white granite. The host granites for tourmaline patches are typically equigranular, and locally porphyritic.

Tourmaline patches contain smoky quartz (>50%; 1-10 mm diameter) intergrown with coarse-grained tourmaline (10-30%; 5-20 mm), K-feldspar (20-30%; 2-10 mm), plagioclase (10-15%; 2-10 mm), and biotite (5-10%; 1-5 mm). Anhedral tourmaline grains are typically interstitial to subhedral quartz and anhedral feldspar (Fig. 3a), and are characterized by vivid red-brown to yellow-green pleochroism under cross polarized light (Fig. 4a). Quartz and K-feldspar grains occur in the massive tourmaline aggregates (Fig. 4b). K-feldspar is volumetrically more abundant than plagioclase in the tourmaline patches, and plagioclase with polysynthetic twins are observed locally within massive tourmaline (Fig. 4a). K-feldspar has irregular contacts with tourmaline, and has typically undergone weak muscovite alteration. Accessory minerals, including anhedral zircon, monazite or titanite, and/or apatite are recognized locally in tourmaline patches (Table 2).

Tourmaline orbicules

Compared with tourmaline patches, the tourmaline orbicules in the Heemskirk and Pieman Heads granites are much larger, ranging from 3 to 15 cm in diameter, and are located near the roof of individual sills (Fig. 2c), where they locally comprise 15-20% by volume of the local granitic body (Figs. 3b, 3g; Table 2). The orbicules are typically characterized by spherical to elliptic shapes (Figs. 3c, 3h). Locally, two or more orbicules are connected to generate larger tourmaline masses (Fig. 3g). Both the red and white phases of Heemskirk Granite have developed tourmaline orbicules, but the orbicules are more common in the white granite.

Tourmaline orbicules are particularly well-developed around the contact between the white and red granites in the Heemskirk Granite at Trial Harbor, where they are mostly hosted by a porphyritic aplite (Fig. 2c). The tourmaline orbicules consist mainly of quartz (> 55%; 1-5 mm) and tourmaline (~ 45%; 0.5-2 mm) with rare muscovite (< 3%). An orbicule-bearing subvertical aplite dyke (20 cm wide) has cut the equigranular white granite (Fig. 3d). The aplite dyke is a feeder to a laterally extensive tourmaline orbicule-rich granitic sill (3 m thick) that overlies the equigranular white granite, and that occurs immediately below the red granite. The tourmaline orbicules in the Heemskirk Granite at Granville Harbor and the Pieman Heads Granite are hosted by equigranular or porphyritic granite (Figs. 3g-h). They typically consist of quartz (35-45%; 0.5-5 mm), tourmaline (30-40%; 0.2-10 mm), K-feldspar (10-20%; 0.5-5 mm), and minor plagioclase (< 10%) and biotite (< 5%). Trace amounts of zircon, monazite, titanite, and or apatite locally occur in the tourmaline orbicules from the two western Tasmanian granites.

Many of the tourmaline orbicules hosted by aplitic granite are internally zoned. Tourmaline is more abundant than quartz in a melanocratic outer zone, whereas a leucocratic inner zone is rich in fine-grained quartz with lesser tourmaline (Fig. 3c). The ovoid outer zone of tourmaline orbicules typically exhibit cryptic, protruding contacts with the neighboring leucocratic host granite (Fig. 3c),

possibly due to high temperature hydrothermal alteration. Tourmalines with deep blue to orange pleochroism (under cross-polarized light) occur in the outer zone. They are 1-2 cm in diameter, and occur as irregular veinlets interstitial to quartz and K-feldspar (Fig. 4c). The inner zone of tourmaline orbicules (5-6 cm) typically displays mosaic textures, where euhedral to subhedral quartz grains are intergrown with massive tourmaline that has greenish-blue to deep blue pleochroism (Fig. 4d). Tourmaline orbicules hosted by equigranular granites in the Heemskirk Granite at Granville Harbor and the Pieman Heads Granite have similar orbicular textures to that formed in tourmaline orbicules from the Seagull Batholith, Yukon Territory, Canada (cf. Sinclair and Richardson 1992). Coarse-grained tourmaline and quartz define the spherical orbicules. The tourmaline-quartz intergrowths are typically rimmed by a 1-3 cm wide leucocratic feldspar-rich halo in the granite (Fig. 3h). Quartz and tourmaline are graphically intergrown in the orbicule.

Tourmaline-filled cavities

The tourmaline-filled miarolitic cavities have diameters varying from 2 cm up to ~~10~~ several meters~~cm~~ (Fig. 3f; Table 2). Tourmaline cavities are concentrated in an upper-level granitic sill within the white Heemskirk Granite at Trial Harbor, and are much less abundant than the orbicules. They occur in both the white and red granites, but are more common in the former. The cavities also occur locally in coarse-grained granite at Granville Harbor.

The tourmaline cavities are characterized by internal growth zones (Fig. 3f), in which columnar tourmaline crystals radiate inwards from the margin to the center of the cavities. The radial tourmaline crystals are intergrown with rare quartz, forming a black central zone from 2 to 6 cm in diameter (Fig. 3f). Klominsky (1972) described these radial tourmaline aggregates as ‘tourmaline suns’. The walls of tourmaline cavities are typically fringed by abundant anhedral quartz with widths of 1-2 cm (Fig. 3f). Anhedral orange-brown to blue pleochroic tourmalines are interstitial to the granular quartz grains (Fig. 4e). These tourmaline crystals typically develop optical zonation patterns

(Fig. 4f) that have not been observed in other tourmaline-textured variants. The centers of the cavities are commonly dominated by planar tourmalines that locally contain subrounded quartz inclusions (Fig. 4e). Narrow altered leucocratic granite halos (several cm wide) typically surround the tourmaline-filled miarolitic cavities, where K-feldspar has been totally or partly replaced by muscovite.

Tourmaline veins

Tourmaline-quartz veins are intensely developed in the apical portions of the Heemskirk and Pieman Heads granites, and have penetrated from the white granite into the overlying red granite at Trial Harbor (Table 2). The veins typically have sub-vertical to vertical orientations (Fig. 3e), and extend up for tens to hundreds of meters from the lowest layer to uppermost region of the exposed pluton. The sub-vertical tourmaline veins have locally cut tourmaline patches and orbicules (Figs. 3e, 3g), indicating that the tourmaline veins are late-stage products of hydrothermal activity.

Tourmaline-quartz veins have internal growth bands, and the adjacent rocks have undergone relatively strong muscovite alteration. These 1-10 cm wide alteration halos consist of prismatic tourmaline, anhedral muscovite (Fig. 4g), and granular to embayed quartz (Fig. 4h). Accessory minerals, such as monazite, xenotime, zircon, titanite, and apatite, have been identified in the tourmaline veins by energy dispersive spectroscopy. They have spongy textures distinct from those accessory minerals crystallized in magmatic environments, and thus may have precipitated from hydrothermal fluids (e.g., Hoskin 2005).

Unidirectional solidification textures

Tens to hundreds of UST-quartz layers occur in the roof zone, and on the margins of the white and red phases of the Heemskirk Granite at Trial Harbor and Granville Harbor, and other locations. The USTs are defined mostly by euhedral quartz crystals up to 5 cm in length. Individual quartz

grains are normally 0.2 to 30 mm in diameter. USTs commonly contain more than one layer of comb quartz, each layer alternating with aplitic granite. A thick quartz UST layer can locally bifurcate into two or more narrow bands. They can extend along a subhorizontal strike for tens to hundreds of meters, but more commonly occur as discontinuous chains.

The quartz-rich UST layers locally contain tourmaline, which is commonly underlain by an aplitic sill enriched in tourmaline orbicules in the apical regions of the white Heemskirk Granite (Fig. 3b). Both sills overlie a domain enriched in tourmaline patches (Fig. 2c). Tourmaline-rich veins have cut quartz-dominated USTs locally. At Trail Harbor, a flat quartz-rich UST layer extends continuously for a few tens of meters, abruptly truncates biotite-rich bands (schlieren) in the red granite, and points downwards into the underlying white granite. This UST provides unambiguous evidence that the red granite was intruded by the underlying white granite sill (cf. Shannon et al. 1982).

Relations between tourmaline-rich features

Tourmaline- and quartz-rich textural features have systematic spatial relationships in the apical portions of sills in the Heemskirk and Pieman Heads granites (e.g., Fig. 2c). At Trial Harbor (Heemskirk Granite), tourmaline orbicules are concentrated in an aplite dyke that fed a granitic sill overlying a tourmaline patch-rich, equigranular granitic layer (Fig. 3d). At Granville Harbor in the Heemskirk Granite, tourmaline orbicules underlie comb quartz-rich USTs that locally contain magnetite, and which are located close to the contact with the Neoproterozoic wall rocks. The miarolitic cavities occur locally below UST layers, but above the tourmaline orbicules (Fig. 3b). At each locality studied, tourmaline veins extend from the lowest exposure level up to the uppermost part of the granite (e.g., Fig. 3g). The veins have locally cut across tourmaline orbicules (Fig. 3e), USTs and/or tourmaline cavities. Figures 2b and 2c systematically illustrate the spatial association of tourmaline-rich features, USTs, and biotite schlieren at Trial Harbor in the Heemskirk Granite.

Based on cross-cutting relationships, tourmaline-quartz veins formed after all of the other tourmaline-bearing textural features. Given that the terminations of USTs typically point downwards to a younger granitic layer (Shannon et al. 1982), tourmaline patches, orbicules, and cavities are therefore interpreted to postdate the overlying USTs. The crystallization relationships between the tourmaline patches, orbicules, and cavities are difficult to ascertain, because no obvious crosscutting or overprinting relationships were observed. At Trial Harbor, tourmaline orbicule-rich aplitic dykes transgress the tourmaline patch-bearing equigranular white Heemskirk granite, implying that the orbicules precipitated later than the tourmaline patches. Tourmaline cavities that occur in a granitic sill overlying the tourmaline orbicules have experienced relatively intense quartz-muscovite alteration. The miarolitic cavities are inferred to have been generated later than the orbicules. The paragenetic sequence of these magmatic – hydrothermal features is therefore interpreted to be USTs → tourmaline patches → orbicules → cavities → veins.

ANALYTICAL METHODS

Electron microprobe analyses

Tourmaline samples, including patches, orbicules, cavities, and veins from the Heemskirk and Pieman Heads granites, were mounted and polished in epoxy resin. Most of the polished planes were oriented perpendicular or parallel to the long axis (c axis) of tourmaline grains. Tourmaline grains were marked for analysis under a normal optical microscope. Backscattered electron images of the selected tourmaline grains were conducted with a FEI Quanta 600 environmental SEM in the Central Science Laboratory at the University of Tasmania (UTAS). Compositional analyses were acquired on a Cameca SX100 electron microprobe equipped with five tunable wavelength dispersive spectrometers in the Central Science Laboratory. Operating conditions were 40 degrees takeoff angle, with beam energy of 15 kV. A probe current of 10 nA and a 10 micrometer diameter beam size were applied during the analytical procedure. The counting time was 10 seconds for Na, Si, K, Cl, 15

seconds for Ca, 20 seconds for Mg, Ti, Ba, Al, P, Mn, Fe, 30 seconds for Sr, Cr, and 45 seconds for F. The detection limits at 3σ above mean background varied from 0.01 to 0.05 wt % for these components with 99 % confidence.

Elements were acquired using analyzing crystals LLIF for Cr, Mn, Fe, PET for Ba, K, Ca, Ti, LPET for Cl, P, Sr, PET for Ba, K, Ca, Ti, TAP for Al, Mg, Na, Si, and PC0 for F. Oxygen was calculated by cation stoichiometry and included in the matrix correction. Oxygen equivalent from halogens (F/Cl/Br/I) was subtracted in the matrix correction. Boron was calculated 0.09677 atoms relative to 1.0 atom of oxygen by stoichiometry. All microprobe analyses of tourmalines were internally calibrated by standard schorl Harvard (E6). In this study, Fe contents are all assumed as Fe^{2+} at the Y-site when calculating the formula of tourmaline. The structural formulae of tourmaline were calculated in an Excel spreadsheet by normalizing to 31 anions including 15 cations in the tetrahedral and octahedral sites (T+Z+Y), and assuming stoichiometric compositions with regard to three B atoms per formula unit (apfu), four (OH+F) apfu (Henry and Dutrow 1996).

Laser ablation ICP-MS analyses

Trace element analyses of tourmalines were acquired by LA-ICP-MS at ARC Centre of Excellence in Ore Deposits (CODES), UTAS. An Agilent 7500cs quadrupole ICP-MS coupled with a Resonetics Resolution S-155 ablation system with a 193nm ArF excimer laser was used in the study. The laser microprobe was equipped with a large format, two-volume ablation cell with the inside holder large enough to fit 20 epoxy rounds. Ablation took place in a helium gas atmosphere flowing at 0.35 l/min carrying the ablated aerosol was mixed with Argon (1.05 l/min) immediately after the ablation chamber. For spot analyses, the aerosol and gas mixture was passed through a pulse-homogenizing device (the “squid” from Laurin Technic, Australia) where the stream of ablated aerosol is split into 10 tubes with differing residence times before being recombined to one tube before entering the ICP-MS plasma. Mineral grains were sampled on 34 micron spots using the laser at 10 Hz and an energy density of approximately 3.5 J/cm^2.

The Excel spreadsheet Laser Template (CODES, UTAS; unpublished) was employed for data reduction which used the NIST612 measured at 89 micron spots as the primary standard for quantification and drift correction. Aluminum was used as the internal standard element for tourmaline as measured by EMPA. External reproducibility was measured on the USGS glass GSD-1g (secondary standard) measured ten times throughout the session, with most elements being below 5% relative standard deviation (RSD), except Be, Cr, Cd, Sn, Au, Tl and Th which are between 6 and 9% RSD (1 σ). The LA-ICP-MS spectra of tourmalines were mostly stable, and thus these spectra were typically chosen to start at 40s and end at 85s during data reduction. In some cases, solid or fluid inclusions in tourmalines were accidently ablated. These spectra have anomalous spikes that were avoided during data processing. Only three analyses were rejected due to contamination by inclusions from a total of 135 LA-ICP-MS analyses of tourmaline. Detection limits for most trace elements were in the range of 0.01 to 0.5 ppm, depending on the element. For some specific elements, the detection limits were typically higher, e.g., 1 ppm for Be, 2 ppm for Cr, 0.68 ppm for Ni, 0.8 ppm for Zn, 1 ppm for Cu, 1.2 ppm for As. The individual external and internal errors for each element measured by LA-ICP-MS are presented in Supplementary[1] Material 3. Li, Ga, Zn, Sn, Sc, Ta, Co, V, Nb, and Ce have average analytical errors below 10 % RSD (1 σ), and Be, P, Pb, Sr, La and Pr between 10 and 24 % RSD (1 σ). The analytical errors of other elements on average exceed 30 %, up to 100 % RSD (1 σ), and their values are mostly below detection limits (Table 5).

Whole-rock chemical analyses

A total of 17 hand-specimen samples were analyzed for their major- and trace-element compositions, including 14 granite rock chips and three tourmaline orbicules from the Heemskirk and Pieman Heads granites (Supplementary Material 1). Samples were analyzed by method code LF200 at ACME Analytical Laboratories Ltd., Vancouver, British Columbia (Canada). Rock samples

[1]Deposit item AM-**-******, Supplemental Material. Deposit items are free to all readers and found on the MSA web site, via the specific issue's Table of Contents (go to http://www.minsocam.org/MSA/AmMin/TOC/).

were crushed, split, and pulverized into 200 meshes, followed by an extra wash with glass between each sample. A total of 66 elements (10 major and 56 trace elements) were analyzed by ICP-MS (inductively coupled plasma-mass spectrometry) and ICP-ES (inductively coupled plasma-emission spectrometry) analytical procedures. 0.2 g sample was split for $LiBO_2/LiB_4O_7$ fusion ICP-ES/ICP-MS analysis, and 0.5 g sample for Ni by 4 acid digestion analyzed by ICP-ES. Detection limits for major and trace elements are presented in Supplementary Material 1.

ANALYTICAL RESULTS

Whole-rock geochemistry

Both the white Heemskirk and Pieman Heads granites are characterized by high SiO_2 (> 73 wt. %) and Al_2O_3 contents (> 12 wt. %), relatively high K_2O (> 4.5 wt. %), and low concentrations of mafic components (Supplementary Material 1). They are strongly peraluminous with alumina saturation index (ASI) values ranging from 1.12 to 1.46, and have moderately high K_2O/Na_2O ratios (1.86 to 2.13). The aplitic phase of white Heemskirk Granite has higher silicic, lower ferromagnesian, and aluminous components than the Pieman Heads Granite. After normalizing trace elements abundances to primordial mantle (McDonough et al. 1992), both the white Heemskirk and Pieman Heads granites display coherent depletions of Ba, Sr, K, and Ti, and enrichments of Cs, Rb, Ta, Pb, and U (Fig. 5a). The Heemskirk Granite contains less of the incompatible elements (e.g., Cs, Ba, Sr, Zr, Ta, Nb, Hf, and Th), and lower rare earth elements than the Pieman Heads Granite (Fig. 5b). The Pieman Heads Granite has intermediate negative Eu anomalies (0.2 to 0.3), and shows a steeper light REE slope than the Heemskirk Granite (Fig. 5b).

Both the white Heemskirk and Pieman Heads granites are classified as strongly fractionated, peraluminous felsic intrusions, based on high Si, Al, K, and Rb/Sr ratios, and low Mg, Fe, and incompatible trace element compositions. These chemical features indicate that the two granitic plutons are typically S-type granites generated by partial melting and/or anatexis of pre-existing

metasedimentary rocks (Scaillet et al. 1995). The Red Heemskirk Granite has lower ASI values (1.0 to 1.17; metaluminous to peraluminous), higher Fe, Mg, and Ca, lower Rb/Sr ratio (7 to 9), and a less fractionated REE pattern than the white granite (Fig. 5b), and is classified as an I-type intrusion.

Compared to their host granites, three analyses of tourmaline orbicules show that they are enriched in Al, Fe, and Mg (Fig. 11a), and moderately to weakly depleted in Na and Ca. They are strongly depleted in K (Fig. 11b), whereas K/Na ratios decrease from 2.0-2.48 in the granites to 0.58-0.91 in the tourmaline orbicules (Supplementary Material 1). Higher concentrations of Al and ferromagnesian elements relate to the presence of abundant tourmaline which also caused the depletion of K, Na, and Ca in tourmaline orbicules. Tourmaline orbicules have noteworthy Ba, Sr, and Pb depletions relative to the host granites (Fig. 5a), due to low contents of feldspar in the orbicules. Although the REE fractionation patterns of tourmaline orbicules are similar to those of their hosts (Fig. 5b), the orbicules have lower REE abundances and more negative Eu anomalies (Fig. 5b), suggesting that they have experienced higher degrees of crystal fractionation.

Backscattered electron imaging of tourmaline growth zones

Compositional zoning patterns in all varieties of tourmalines have been examined using scanning electron microscope-backscattered electron (SEM-BSE) images. In general, three types of compositional zones have been recognized: (1) oscillatory zoning, (2) concentric zoning, and (3) radial zoning (Fig. 6). Hourglass zones in sections parallel to the c-axis described in metamorphic tourmaline (e.g., van Hinsberg et al. 2006) are absent in the tourmalines from western Tasmanian granites.

Oscillatory zoning patterns have mainly been identified in tourmaline grains from cavities and veins. This type of zoning typically defines a dull grey core rimmed by bright, alternating intergrowths in SEM images (Figs. 6a-d). In contrast, concentric zoning patterns are defined by a simple dull grey core surrounded by a bright rim, in which alternating growth zones are absent (Figs. 6e-g). Concentric growth zones have been observed in all of the tourmaline-rich features. Minor

radial zoning patterns (Figs. 6h, i) have been detected in tourmaline from orbicules and patches. The radial zones are defined by light grey laths intergrown with dark grey laths. Radial zoning is somewhat similar to the bright and dark grey rims of oscillatory zoned tourmaline. The observed compositional zoning patterns have been influenced by the orientations of the section cut through individual tourmaline crystals (cf. van Hinsberg et al. 2006). The oscillatory zoning and concentric zoning patterns are apparent on planes perpendicular or parallel to the c-axis, whereas radial zoning patterns are largely observed in sections oblique to the long (c) axis. Because sections perpendicular or parallel to the c axis are the best planes to depict the zoning features of tourmalines, concentric and oscillatory zoning patterns are considered to be most indicative of the compositional zones of tourmaline crystals in the western Tasmanian granites.

EMPA results of tourmaline

A total of 347 electron microprobe analyses have been obtained from tourmaline crystals. The average compositions of tourmalines from different locations are tabulated in Table 3, and the detailed results for each analysis are documented in Supplementary Material 2. According to the nomenclature of Henry et al. (2011), most of the tourmalines belong to the alkali group, and a few belong to the X-site vacant group, with (Na + K) > 0.5 apfu, $^{X}\square \approx 0.5$ apfu, and Ca < 0.1 apfu (Supplementary Material 2). These tourmalines are Fe-enriched at the Y-site, and plot mostly in the schorl field, overlapping slightly with the foitite field (Fig. 7). The average mole fractions of end-member compositions of tourmalines from the Heemskirk and Pieman Heads granites are tabulated in Table 4, and were calculated using the Excel spreadsheet of Morgan (2016).

Tourmalines in the Heemskirk Granite from Trial Harbor were analyzed from patches, orbicules, cavities, and veins, while only tourmalines from orbicules and cavities were measured from Granville Harbor. Tourmaline grains in the Heemskirk Granite at Trial Harbor and Granville Harbor display mean mole fractions of end-member components of $schorl_{51}$ $dravite_{4}$ $Fe\text{-}uvite_{3}$ $foitite_{30}$

Mg-foitite$_2$ olenite$_8$ and schorl$_{46}$ dravite$_6$ Fe-uvite$_3$ foitite$_{31}$ Mg-foitite$_4$ olenite$_9$ (Table 4), respectively. The tourmalines have similar compositions, with Fe/(Fe + Mg) ratios (abbreviated as #Fe) ranging from 0.82 to 1.0 (Fig. 7a). Tourmaline grains at Granville Harbor have lower #Fe values than tourmalines from equivalent textures at Trial Harbor (Fig. 7a). Aluminum, Na, Ti, and F have similar concentrations from both sites (Figs. 7, 8). The linear relationship in the Mg-Fe plot (Fig. 8a; r^2 = 0.22) indicates that schorl-dravite substitution plays an important role in the Heemskirk tourmalines ($FeMg_{-1}$ vector; Henry et al. 2011). The values of $\sum$(Fe + Mg) < 3 apfu suggest that substantial accounts of Al (up to 0.73 apfu) have been incorporated into the Y-site. Al^{3+} is able to substitute for Fe^{2+}, Mg^{2+}, and Mn^{2+} at the Y-site (Fig. 8c), with a vacant X-site maintaining charge balance. This substitution relates to the vector $^{Y}Al\ ^{X}\square(R^{2+}Na)_{-1}$ where R^{2+} = (Fe + Mg + Mn). A number of deviations from the $^{Y}Al\ ^{X}\square(R^{2+}Na)_{-1}$ exchange trend are apparent in the total Al versus $^{X}\square$ plot (Fig. 8c), which accounts for the $^{Y}AlO(R^{2+}OH)_{-1}$ substitution (Henry et al. 2011). The tourmalines contain minor Ti values at the Y-site (0.01 to 0.11 apfu) which decrease with increasing #Fe values (r^2 = 0.46; Fig. 7b). F contents at the W-site fluctuate significantly from 0.05 to 0.75 apfu, and many of the tourmalines are fluor-schorls due to #Fe > 0.5 and F > 0.5 apfu (Henry et al. 2011). Manganese, Ca, and K are minor components of tourmalines from the Heemskirk Batholith, generally lower than 0.05 apfu.

Compared with the Heemskirk Batholith, tourmalines associated with the Pieman Heads Granite are relatively enriched in Mg, and depleted in Fe and Na, and thus have a wider range of #Fe values (0.65 to 0.99). These tourmalines possess an average mole fraction of end-member compositions of schorl$_{35}$ dravite$_9$ Fe-uvite$_2$ foitite$_{32}$ Mg-foitite$_8$ olenite$_{11}$ (Table 4). More tourmalines thereby have been classified as foitites on the Fe/(Fe + Mg) and $^{X}\square$/(Na + K + $^{X}\square$) diagram (Fig. 7c), with some classified as part of the oxy-foitite group (Fig. 8b). According to the Mg versus Fe and total Al versus $^{X}\square$ plots (Figs. 8b, 8d), the compositional variations of tourmalines from this granite are jointly constrained by $FeMg_{-1}$, $^{Y}Al^{X}\square(R^{2+}Na)_{-1}$, and minor $^{Y}AlO(R^{2+}OH)_{-1}$ substitution mechanisms. Some

tourmalines in veins at Pieman Heads have moderately deviated from the known exchange vectors above (Figs. 8b, 8d). These anomalous tourmalines exhibit extraordinary enrichment of Mn contents (0.19 to 0.34 apfu), one order of magnitude higher than all other tourmalines (Mn < 0.05 apfu; Fig. 9). Al in Y-site increases with Mn for Mn-rich tourmalines (Fig. 9), which cannot account for the $^{Y}Al^{X}\square(R^{2+}Na)_{-1}$ and $^{Y}AlO(R^{2+}OH)_{-1}$ exchanges (Fig. 8d). This probably indicates the existence of additional exchange mechanism, e.g., a $FeMn_{-1}$ vector. These tourmalines are also characterized by comparatively higher ^{Y}Al ($\approx$ 1 apfu), with substantial depletion of Fe (~1.5 apfu) and Mg (< 0.1 apfu).

Tourmalines from the Pieman Heads and Heemskirk granites have similar major element variations between different tourmaline-rich features (Figs. 7, 8). Tourmaline in patches tends to have the highest Mg and Ti, and lowest Fe, whereas tourmaline in veins has the highest Fe, and lowest Mg and Ti contents. These elements in tourmaline from orbicules and cavities plot in the middle of the field defined by patches and veins. Al and Na contents in tourmaline from different features largely overlap (Figs. 7, 8). The variation patterns of Fe/Mg and Al in tourmalines from the two western Tasmanian granites contrast with those in tourmalines within the leucogranites at Cornwall (SW England), probably indicating the hydrothermal vein tourmalines in this study were not heavily contaminated by Fe-Mg components derived from the wallrocks (cf. London and Manning 1995). Intense tourmalization of the Oonah Formation country rocks has occurred to the north of the Heemskirk Granite, but the wallrock-hosted tourmaline was not sampled or analyzed in our study.

LA-ICP-MS results of tourmaline

More than 40 trace elements in tourmaline from the western Tasmanian granites have been analyzed by LA-ICP-MS. The ranges and medians of these elements are documented in Table 5, whereas the detailed data for each analysis are tabulated in Supplementary Material 3. The median concentrations for most trace elements range from 0.1 to 10 ppm. Lithium, Zn, and Ga have the

highest median concentrations, up to hundreds of ppm. Vanadium, Co, Sc, P, and Sn show median values of tens of ppm. Chromium, Ni, Ta, Nb, Sr, Pb, and light REEs have median concentrations of several ppm, whereas heavy REEs, Rb, Y, Mo, Cs, Sb, Ba, Hf, W, Au, Bi, Th, and U have median concentrations < 1 ppm (Table 5). Many trace elements have large variations over several orders of magnitude in concentrations (Table 5). A number of trace elements have concentrations below detection limit (bdl), and the percentages of analyses of individual elements that are bdl range from 0 to 96 % (Table 5).

Lithium and Be concentrations in tourmalines from the Pieman Heads Granite have a broader range than those from the Heemskirk Batholith, although tourmalines in the Heemskirk Batholith have higher mean Li and Be contents (Fig. 10). The tourmalines at Granville Harbor have the narrowest range (74.6 to 154.3 ppm) but the highest median (131.4 ppm) for Li content. Most transition elements, e.g., Sc, V, Co, and Ni, are preferentially enriched in tourmaline from the Pieman Heads Granite relative to the Heemskirk Batholith (Fig. 10).

The most enriched trace elements in tourmaline are Zn and Ga, up to 420 and 790 ppm, respectively (Table 5). They have similar mean values in the Heemskirk and Pieman Heads granites, but the highest values for both elements are from the latter pluton. Large ion lithophile elements (LILEs) exemplified as Sr and Pb exhibit significant variations from < 1 to several ppm, or rarely to tens of ppm. They are depleted in tourmaline from the Heemskirk Batholith compared to the Pieman Heads Granite. Most REEs were undetectable in tourmaline grains, except for La, Ce, Pr, and Nd. These REEs are typically enriched in tourmaline from the Heemskirk Batholith. Similarly, high field strength elements (HFSEs), such as Ta, Nb, Zr, Hf, and Th, have consistently higher concentrations in tourmaline from the Heemskirk Batholith (Fig. 10).

Tin concentrations up to 280 ppm were detected in tourmalines from the Sn-mineralized Heemskirk Batholith. These values are much higher than the median concentrations in tourmalines from the barren Pieman Heads Granite (13.7 ppm; Table 5). Most of the high Sn values in

tourmalines come from the Heemskirk Batholith at Trial Harbor (Fig. 10). A few tourmaline grains contain anomalously high Sn contents in tourmaline veins at Pieman Heads. The mean Sn concentrations in tourmalines from the Heemskirk Batholith at Granville Harbor and Pieman Heads Granite are similar to those of the corresponding whole-rock compositions (Fig. 10).

Tourmaline preferentially incorporates transition elements (e.g., Zn, Co; cf. Henry and Dutrow, 2001), together with Li, Be, and Sn, compared to their host granites (Fig. 11a). This may be due to substitutions for major elements in tourmaline (e.g., Fe, Al, and Na), because these elements have similar atomic radii and charges (e.g., Henry et al. 2011). The tourmalines are slightly depleted in HFSEs (e.g., Nb, Ta), and significantly depleted in LILEs (e.g., Sr, Pb) and REEs relative to their host granites (Fig. 11b).

Compositional variations between tourmaline sector zoning

In BSE images that show zoning in tourmalines from the two granites, the concentric cores of tourmaline are mostly c-sectors (cf. Marks et al. 2013), whereas the outer zones and oscillatory rims are inferred to correspond to a-sectors (Fig. 6). Typical triangular o-faces and banded r-faces (pyramidal faces; cf. van Hinsberg et al. 2006) have been found in some c-sector planes (e.g., Fig. 6c), but they are uncommon. The c^--sectors display bright inner cores (e.g., Fig. 12c), whereas dark cores of sector zonings are inferred as c^+-sectors (Figs. 6a-d; van Hinsberg et al. 2006).

Figure 12 shows representative analytical profiles for tourmaline grains with sector zones based on combined EMPA and LA-ICP-MS results. Compositional variations in tourmaline growth zones from the Pieman Heads Granite are similar to those from the Heemskirk Batholith. However, Fe- and Al-rich cores have been only observed in Pieman Heads tourmalines (Fig. 12d).

Compositional profiles show that most major and trace elements in western Tasmanian tourmaline grains have different substitutions in the c-and a-sectors (Fig. 12). When compared to the neutral a-sector (Henry et al. 1999; van Hinsberg et al. 2006), the c^+ -sector is enriched in Al and the

X-site vacancies, and depleted in Fe, Mg, Ca, Na, K, Ti, and F (Fig. 12). The c$^-$-sector appears to be enriched in Al, Fe, Ca, and K compared to the a-sector, but lower in Mg, Ti, Na, and F (e.g., Fig. 12c). Within the zoned cores (c-sector), the wedge-shape o-face is commonly depleted in Fe, Na, and Ca, but enriched in Al^Y, Mg, and X-site vacancies relative to the laminated r-face (e.g., Fig. 12c). Most trace elements from individual tourmaline grains show variable enrichments and depletions between the c- and a-sector zones (Fig. 12). Zn and Ga do not have any strong preference in each sector zone. Lithium, Sr, Pb, and REEs are more enriched in the a-sector, whereas the c-sector has pronounced enrichments of Co, Ni, V, Sc, and Th. Beryllium, Sn, Hf, and Zr concentrations are enriched in the c-sector, whereas Cr, Ta, and Nb are higher in the a-sector (Fig. 12). These gradual compositional variations from core to rim may relate to the different growth rates of individual faces of tourmaline that produces preferential incorporation of elements on specific growth planes (Henry et al. 1999; van Hinsberg et al. 2006).

Some tourmaline grains have dramatic intra-crystalline variations, with a-sector/c-sector ratios up to 10 (e.g., Fig. 12d). The exceptionally Mn- and Al-rich tourmaline core from quartz veins at Pieman Heads contains the highest Al, Mn, X-site vacancies, Li, Zn, Ga, Sc, and Sn, and the lowest Fe, Mg, Ca, Co, Ni, Sr, Pb, V, REEs, Ta, and Nb among the three tourmaline growth zones (Fig. 12d). The concentrations of these elements change dramatically between the core and bright inner rim, up to several orders of magnitude, contrasting to the gradual variations between the bright inner and grey outer tourmaline rims (Fig. 12d). The tourmaline core shows an apparent dissolution-recrystallization texture along its contacts with the inner rims (Fig. 12d). Irregular apatite grains containing zircon micro-inclusions define the boundary of the core and rim of this tourmaline grain (Fig. 6c). These chemical and mineralogical features imply that the Al-Mn-rich core and Fe-Mg-rich rim tourmalines precipitated from multiple-stages of fluids with distinctive compositions.

DISCUSSION

Influence of bulk composition of the host rocks

Chemical variations of tourmaline crystals are influenced both by internal factors (e.g., crystallographic sectors), and external factors such as the bulk composition of the host rock, composition of coexisting minerals and fluids, and P-T-fO_2 conditions (Henry and Guidotti 1985; van Hinsberg et al. 2011a, 2011b; Dutrow and Henry 2011; Marks et al. 2013). In order to diminish the effect of intra-crystalline partition of trace elements, it is best to compare trace elements from the neutral a-sector (van Hinsberg et al. 2006) when assessing external influences on tourmaline chemistry (Marks et al. 2013). For the western Tasmanian tourmalines, there are few differences between the a-sector data and the c-sector data (except for several anomalous results; Fig. 12d), and chemical variations related to sector zoning are subordinate to those related to variations in host rocks and geographic locations (e.g., Figs. 10, 13).

The chemical compositions of tourmaline crystals from western Tasmanian granites plot mostly in the Li-poor granitoid field, with a few in the Li-rich granitoid field in the ternary Al-Fe-Mg diagram of Henry and Guidotti (1985; Fig. 13). The contents of Al, Mg, and most transition elements (e.g., Sc, V, Co, and Ni), large ion lithophile elements (e.g., Pb and Sr), and REEs are elevated in the Pieman Heads tourmalines compared to those from the Heemskirk Batholith (Fig. 14).

Tourmalines from the Heemskirk batholith are enriched in Sn, Na, and most high field strength elements (e.g., Ta, Nb, Zr, Hf, and Th) relative to tourmalines associated with the Pieman Heads Granite (Fig. 14). Chemical heterogeneities between tourmalines are comparable to the differences in whole-rock compositions between the two granitic intrusions (Fig. 10). The major and trace element abundances of the tourmaline crystals are considered to be most strongly controlled by their granitic hosts, to a greater extent than by the effect of sector zoning crystallography (Fig. 10). This conclusion is in agreement with the assertion that tourmaline chemistry mostly reflects the compositional nature of its host melt and/or fluid (van Hinsberg 2011).

Volatile exsolution influence between different textural variants of tourmalines

Post-magmatic metasomatic alteration related to boron-rich hydrothermal fluids derived from the crystallizing granites along fractures has been proposed for the genesis of tourmaline nodules in felsic granites (Dick 1980; Le Fort 1991; Rozendaal and Bruwer 1995). The tourmaline patches and orbicules are commonly distributed in the upper parts of granites as disseminated masses or clusters. There is abundant field evidence that later tourmaline-filled fractures have cut across the orbicules (e.g., Fig. 3e), disproving the hypothesis that veins play a role as conduits to feed or recharge the orbicules (cf. Dick 1980; Le Fort 1991; Rozendaal and Bruwer 1995). The observed cross-cutting relationships contradict the genetic model that tourmaline orbicules result from post-magmatic alteration by boron-rich fluids migrating along fractures. Nonetheless, the observed leucocratic outermost rims of the orbicules contain anhedral secondary muscovite and tourmaline, and K-feldspar relicts that are unambiguously caused by hydrothermal alteration, implying a hydrothermal contribution to orbicule formation.

Tourmaline orbicules have been alternatively interpreted to be magmatic – hydrothermal features resulting from devolatilization and phase separation of hydrous boron-rich fluids unmixed from granitic melts (Sinclair and Richardson 1992; Samson and Sinclair 1992; Jiang et al. 2003; Shewfelt 2005; Buriánek and Novák 2007; Dini et al. 2007; Perugini and Poli 2007; Trumbull et al. 2008; Balen and Broska 2011; Drivenes et al. 2015). These fluids were trapped beneath the roof of crystallizing granitic sills, and also formed unidirectional solidification textures (cf. Shannon et al. 1982). This model best explains the origins of tourmaline-rich features formed in the western Tasmanian granites.

Volatile-rich hydrous phases can exsolve from the crystallizing melts during emplacement into the shallow crust due to phase separation (Burnham 1979). In felsic magmas formed by partial melting of metapelitic rocks, boron has extremely incompatible behavior (London et al. 1996). It can

be concentrated within silicic melts, but will eventually be further partitioned into a bubble-rich aqueous phase (London et al. 1996; Dingwell et al. 1996). Experimental studies have shown that during fractional crystallization of silicic magmas, a B-Fe-Na-rich aqueous phase can separate from the initial aluminosilicate-rich and water-rich melts due to liquid immiscibility (Veksler and Thomas 2002; Veksler 2004). The ASI of the investigated white Heemskirk and Pieman Heads granites (mostly 1.18 to 1.46), high boron contents (based on widespread tourmaline in the granites), estimated lithostatic pressures of 1 to 1.2 kbar (4 to 5.5 km depth) and temperatures of 600-700 °C (Hajitaheri 1985), and relatively high fluorine concentrations (EMPA on tourmaline) fall largely into the field of tourmaline stability suggested by Wolf and London (1997) and London (1999). It might be that a B-Fe-Na-rich aqueous phase separated before complete crystallization of biotite, cordierite and garnet – which is supported by absence of biotite in the granitic regions surrounding the tourmaline orbicules (Figs.3c, d, h), leading to a significant proportion of ferromagnesian components being available to generate the tourmaline crystals (cf. Drivenes et al. 2015). The huge volume of tourmaline developed over the 20 × 30 km areal exposure of the Heemskirk Granite shows that this intrusion was very capable of crystallizing tourmaline.

Continuous decompression during crystallization of the hydrous magmas can give rise to a spanning cluster of bubbles of volatiles (Burnham 1979; Candela 1991; Fig. 15a). Petrographic observations of fluid inclusions have shown that salt-bearing fluid inclusions coexist with liquid-rich fluid inclusions in quartz from the tourmaline orbicules (Hajitaheri 1985). A hypersaline fluid exsolved from a granitic melt had the potential to transport significant concentrations of Fe, Mg and Na. Furthermore, Al can be highly soluble if the brine is acidic (e.g., Seedorff et al. 2005). Incompatible boron will have been preferentially transported in vapor bubbles, as the B-Fe-Na-rich brine and coexisting vapor ascended of to the cupolas of the intrusion. The bubble-laden plume theory (Candela 1991) can explain the transport of a buoyant Fe (Mg)-Na-(Al)-rich brine and B-rich vapor exsolved from a granitic melt.

Buoyant volatile bubbles can be released from a crystallizing melt at low degrees of crystallization, and are transported upwards between grain boundaries in the manner of bubble-laden plumes or tubules (Candela 1991, 1997; Fig. 15b). As magma crystallization proceeds and the viscosity increases, small bubbles may coalesce to form tube flows during their journey to the apical regions of the intrusion. The bubbles may freeze out as miarolitic cavities if the abundance of volatiles is too low to form a spanning cluster. When the volatile supply diminishes, the bubble-laden plume ultimately collapses, producing irregular patches coexisting with coarse-grained igneous crystals. At high degrees of crystallization, the bubbles are more likely to be trapped into pockets of peripheral magma because capillary forces can drive abundant water and volatiles adhering to the crystal mush of alumino-siliceous components (Shinohara and Kazahaya 1995; Harris et al. 2004). These buoyant bubbles can gradually percolate through the crystal mush, and at higher degrees of magma crystallization, will coalesce to grow larger until overcoming the capillary force, typically occurring as spherical or elliptical shapes in order to reduce surface energy. When the magma cools down, large stagnant bubbles that contain significant alumino-siliceous elements will not collapse, unlike the small bubbles that occur interstitially to grain boundaries. The large bubbles will be trapped separately as spherical, subround or ellipsoidal bodies in felsic intrusions (Fig. 15c). Diffusion of fluids from the bubbles into the surrounding granite during its solidification is likely to have produced the altered rims commonly observed around most of the tourmaline orbicules and cavities (e.g., Figs. 3c, 3f, and 3h).

The irregular tourmaline patches disseminated in western Tasmanian granites are interpreted to be tourmalinized remnants of granites that contained the small boron-rich volatile bubbles (Fig. 15b), whereas the spherical tourmaline orbicules and cavities solidified in uppermost portions of the granites are likely to be relicts of large trapped volatile bubbles enriched in B, Fe, Al, and Na that reactivated with the melt (Fig. 15c). Tourmaline grains from orbicules and cavities contain higher Fe, volatiles (Li, Be), and incompatible elements (Nb, Ta, Th, U, and Pb), but lower Mg, Na, Ti, and

transition elements (V, Co, Sc, Zn, and Ga) than the tourmaline patches (Fig. 14). Strontium contents have been found to increase with incompatible elements (Nb, Ta, Th, U, and Pb) and volatile elements (F, Li, Be) in the transition from tourmaline patches to orbicules and cavities (Fig. 14). This may be because high volatile contents (e.g., F) can promote significant Sr being preferentially incorporated into an aqueous phase (Hannah and Stein, 1990). Nevertheless, these chemical variations imply that the magmatic – hydrothermal fluids evolved compositionally, largely due to progressive crystal fractionation and high volatile contents of the parental intrusion.

Compared to other tourmaline-rich features, tourmalines from quartz-tourmaline veins in western Tasmanian granites are relatively depleted in Na, Mg, Ti, and Ca as well as transition elements (V, Co, Sc, Zn, and Ga). They are enriched in Fe, Al^{Y}, Be, Sr, and incompatible elements (e.g., Nb, Ta, Pb, and REEs; Figs. 8, 14). The quartz-tourmaline veins precipitated from a boron-rich aqueous fluid. During the final stage of granite crystallization and emplacement, large amounts of boron-rich aqueous fluids are intended to have accumulated at the interface between the tourmaline orbicule-bearing carapace and underlying crystallizing magma (Fig. 15). Increasing vapor pressure exceeded lithostatic pressure, leading to the fracture failure of the carapace and neighboring wallrocks. Boron-rich aqueous fluids migrated along these fractures, hydrothermally altering the host rocks, and eventually sealing the veins by mineral precipitation (e.g., Burnham 1979; Fig. 15d). The veins locally cut early-formed tourmaline orbicules (e.g., Fig. 3e). Cycles of hydro-fracturing generated multiple phases of tourmaline-filled quartz veins (cf. Dini et al. 2008).

Implications for Sn enrichment and mineralization

Some tourmaline orbicules in the Heemskirk Batholith reportedly contain cassiterite (Waterhouse 1916). Subsequent studies only found a few cassiterite grains in quartz-tourmaline veins, and not in the tourmaline orbicules (Klominsky 1972; Hajitaheri 1985). No cassiterite has been found to occur within tourmaline orbicules, cavities or veins among more than 50 thin sections and

mounts examined in this study. This is partly because our sample locations are ca. 1 km from the nearest historical Sn workings in the Heemskirk Granite at Trial Harbor (Fig. 2a). Whole-rock analyses of tourmaline orbicules show that their Sn contents are commonly higher than the granite host rocks (Fig. 11a). Tin is more abundant in orbicules from the Heemskirk Batholith at Trial Harbor than from Pieman Heads Granite. The white Heemskirk intrusion is more felsic and highly fractionated than the Pieman Heads Granite, with Rb/Sr ratios for the Heemskirk Batholith several times higher than those for the Pieman Heads Granite. High degrees of fractional crystallization are important for concentrating Sn in felsic magmas (Blevin and Chappell 1992, 1995). Variable extents of fractionation crystallization led to the different concentrations of Sn between these two intrusions.

Volatile components of the crystallizing magmas play a vital role in the formation of magmatic – hydrothermal mineral deposits. The volatiles can increase metal solubilities and decrease melt viscosities, and facilitate metal transport at high concentrations in magmatic – hydrothermal fluids (Hedenquist and Lowenstern 1994; Cooke et al. 2009). Tourmaline contains substantial volatile components (e.g., B, F, and Li), and it is commonly viewed as a liquidus phase in felsic magmas (Benard et al. 1985; Dingwell et al. 1996). Because tourmaline orbicules and associated tourmaline-rich features are the consequences of volatile exsolution from the crystallizing intrusion, they have been able to concentrate Sn during granite crystallization at Trial Harbor and to a lesser content at Granville Harbor. As a result, high Sn (up to 280 ppm), together with elevated Fe, Be, Ta, Nb, Sr, and REEs, and lower Mg, Ti, Sc, V, Cr, and Co, were incorporated into tourmalines in the cavities and veins in the white Heemskirk Granite at Trial Harbor.

Element ratios between enriched and depleted elements in tourmaline can amplify geochemical anomalies inherited from the host granites. Geochemical diagrams that plot element ratios (e.g., Zn/Nb, Co/Nb, Sr/Ta, and Co/La) against Sn concentrations in tourmaline clearly separate the Sn-mineralized intrusion (Heemskirk Granite at Trial Harbor) from the barren granite (Pieman Heads Granite) from western Tasmania (Fig. 16). Element ratios and Sn contents in tourmaline from the

Heemskirk Granite at Granville Harbor are situated in intermediate districts on these discriminative diagrams, partially overlapping with the Trial Harbor and Pieman Heads data (Fig. 16). Trace element ratios plotted against Sn from tourmaline may therefore prove to be powerful tools to discriminate productive and barren tin granites (Fig. 16).

IMPLICATIONS

Distinctive magmatic – hydrothermal features, including tourmaline patches, orbicules, cavities, and veins, have typically developed in discrete layers in the roof of individual granitic sills of the Heemskirk and Pieman Heads granites from western Tasmania, particularly at the contact between the white and red phases of the Heemskirk Granite. These tourmaline grains commonly display distinctive compositional growth zonation patterns revealed by backscattered electron imaging.

Magmatic – hydrothermal volatile exsolution and fluxing of boron-rich aqueous fluids evolved from the crystallizing granitic magmas during the emplacement into shallow crust are ascribed to the formation of these tourmaline-rich textural features. The chemical variations in tourmaline from the Heemskirk and Pieman Heads granites are predominantly determined by the relative compositional differences between their host rocks. Elemental diagrams that Zn/Nb, Co/Nb, Sr/Ta, and Co/La plot against Sn concentrations in tourmaline are proposed as discriminators to explore Sn-mineralized granites from barren intrusions.

ACKNOWLEDGEMENTS

We would like to thank ARC Centre of Excellence in Ore Deposits (CODES), University of Tasmania for granting a PhD scholarship to the primary author (W. Hong). An ARC Centre of Excellence-linking fund (P2.A3A) and the Hugh E. McKinstry Fund from Society of Economic Geologists provided financial support that made this study possible. Stephanie Sykora is thanked for helping W. Hong to map the tourmaline-rich features in the field. Dr. Karsten Goemann and Dr.

Sandrin Feig from Central Science Laboratory, University of Tasmania, are acknowledged for assisting with BSE imaging and microprobe analysis.

REFERENCES CITED

Balen, D., and Broska, I. (2011) Tourmaline nodules: products of devolatilization within the final evolutionary stage of granitic melt? Geological Society, London, Special Publications 350, 53–68.

Benard, F., Moutou, P., and Pichavant, M. (1985) Phase relations of tourmaline leucogranites and the significance of tourmaline in silicic magmas. The Journal of Geology, 93, 271–291.

Berry, R.F., and Crawford, A.J. (1988) The tectonic significance of Cambrian allochthonous mafic-ultramafic complexes in Tasmania. Australian Journal of Earth Sciences, 35, 523–533.

Black, L.P., McClenaghan, M.P., Korsch, R.J., Everard, J.L., and Foudoulis, C. (2005) Significance of Devonian–Carboniferous igneous activity in Tasmania as derived from U–Pb SHRIMP dating of zircon. Australian Journal of Earth Sciences, 52, 807–829.

Blevin, P.L., and Chappell, B.W. (1992) The role of magma sources, oxidation states and fractionation in determining the granite metallogeny of eastern Australia. Transactions of the Royal Society of Edinburgh: Earth Sciences, 83, 305–316.

——1995, Chemistry, origin and evolution of mineralized granites in the Lachlan Fold Belt, Australia: the metallogeny of I- and S-type granites. Economic Geology, 90, 1604–1619.

Both, R.A., and Williams, K.L. (1968) Mineralogical zoning in the lead-zinc ores of the Zeehan field, Tasmania Part I: Introduction and review. Journal of the Geological Society of Australia, 15, 121–137.

Buriánek, D., and Novák, M. (2007) Compositional evolution and substitutions in disseminated and nodular tourmaline from leucocratic granites: Examples from the Bohemian Massif, Czech Republic. Lithos, 95, 148–164.

Burnham, C.W. (1979) Magmas and hydrothermal fluids. In H.L. Barnes, Ed., Geochemistry of Hydrothermal Ore Deposits: 2nd ed., p. 71–136. Wiley, New York.

Candela, P.A. (1991) Physics of aqueous phase evolution in plutonic environments. American Mineralogist, 76, 1081–1091.

——(1997) A review of shallow, ore-related granites: textures, volatiles, and ore metals. Journal of Petrology, 38, 1619–1633.

Cooke, D.R, Kitto, P.A., Harris, A.C., Chang, Z., Wilkinson, J.J., Wilkinson, C.C., Hollings, P., and Webster, J.D. (2009) Magma fertility and mineralization. In Smart Science for Exploration and Mining-Proceedings of the 10th Biennial SGA Meeting, v.1, p. 8–10. Economic Geology Research Unit, Townsville.

Cooke, D.R., Baker, M., Hollings, P., Sweet, G., Chang, Z., Danyushevsky, L., Gilbert, S., Zhou, T., White, N., Gemmell, J.B., and Inglis, S. (2014) New advances in detecting the distal geochemical footprints of porphyry systems—epidote mineral chemistry as a tool for vectoring and fertility assessments. Society of Economic Geologists, Special Publication 18, 127–152.

Dick, L.A. (1980) A comprehensive study of the geology, mineralogy and conditions of formation of contact metasomatic mineral deposits in the Northeastern Canadian Cordillera, Ph.D. thesis, Queen's University, Kingston, Ontario.

Dingwell, D.B., Pichavant, M., and Holtz, F. (1996) Boron in granitic rocks and their contact aureoles. In L.M. Anovitz, and E.S. Grew, Eds., Boron: Mineralogy, petrology and geochemistry, 33, p. 299–330. Reviews in Mineralogy and Geochemistry, Mineralogical Society of America, Chantilly, Virginia.

Dini, A., Corretti, A., Innocenti, F., Rocchi, S., and Westerman, S. (2007) Sooty sweat stains or tourmaline spots? The Argonauts on the Island of Elba (Tuscany) and the spread of Greek trading in the Mediterranean Sea. Geological Society, London, Special Publications 273, 227–243.

Dini, A., Mazzarini, F., Musumeci, G., and Rocchi, S. (2008) Multiple hydro-fracturing by boron-rich fluids in the Late Miocene contact aureole of eastern Elba Island (Tuscany, Italy). Terra Nova, 20, 318–326.

Drivenes, K., Larsen, R.B., Müller, A., Sørensen, B.E., Wiedenbeck, M., and Raanes, M.P. (2015) Late-magmatic immiscibility during batholith formation: assessment of B isotopes and trace elements in tourmaline from the Land's End granite, SW England. Contributions to Mineralogy and Petrology, 169:56. DOI 10.1007/s00410-015-1151-6.

Dutrow, B.L., and Henry, D.J. (2011) Tourmaline: A Geologic DVD. Elements, 7, 301–306.

Green, G.R. (2012) Ore deposits and metallogenesis of Tasmania. Episodes, 35, 205–215.

Griffin, W.L., Slack, J.F., Ramsden A.R., Win, T.T., and Ryan, C.G. (1996) Trace elements in tourmaline from massive sulfide deposits and tourmalinites: geochemical controls and exploration applications. Economic Geology, 91, 657–675.

Hajitaheri, J. (1985) The origin of mineralisation in South Heemskirk granite, Western Tasmania, Australia, 322 p. Ph.D. thesis, University of Tasmania, Hobart.

Halpin, J.A., Jensen, T., McGoldrick, P., Meffre, S., Berry, R.F., Everard, J.L., Calver, C.R., Thompson, J., Goemann, K., and

Whittaker, J.M. (2014) Authigenic monazite and detrital zircon dating from the Proterozoic Rocky Cape Group, Tasmania: Links to the Belt-Purcell Supergroup, North America. Precambrian Research, 250, 50–67.

Hannah, J.L., and Stein, H.J. (1990) Magmatic and hydrothermal processes in ore-bearing systems. Geological Society of America, Special Paper 246, 1–10.

Harris, A.C., Kamenetsky, V.S., White, N.C., and Steele, D.A. (2004) Volatile phase separation in silicic magmas at Bajo de la Alumbrera porphyry Cu-Au deposit, NW Argentina. Resource Geology, 54, 341–356.

Hedenquist, J.W., and Lowenstern, J.B. (1994) The role of magmas in the formation of hydrothermal ore deposits. Nature, 370, 519–527.

Henry, D.J., and Dutrow, B.L. (1996) Metamorphic tourmaline and its petrologic applications. In L.M. Anovitz, and E.S. Grew, Eds., Boron: Mineralogy, petrology and geochemistry, 33, p. 503–557. Reviews in Mineralogy and Geochemistry, Mineralogical Society of America, Chantilly, Virginia.

Henry, D.J., and Dutrow, B.L. (2001) Compositional zoning and element partitioning in nickeloan tourmaline from a metamorphosed karstbauxite from Samos, Greece. American Mineralogist,1130–1142.

Henry, D.J., and Guidotti, C.V. (1985) Tourmaline as a petrogenetic indicator mineral: an example from the staurolite-grade metapelites of NW Maine. American Mineralogist, 70, 1–15.

Henry, D.J., Kirkland, B.L., and Kirkland, D.W. (1999) Sector-zoned tourmaline from the cap rock of a salt dome. European Journal of Mineralogy, 11, 263–280.

Henry, D.J., Novák, M., Hawthorne, F.C., Ertl, A., Dutrow, B.L., Uher, P., and Pezzotta, F. (2011) Nomenclature of the tourmaline-supergroup minerals. American Mineralogist, 96, 895–913.

Hoskin, P.W.O. (2005) Trace-element composition of hydrothermal zircon and the alteration of Hadean zircon from the Jack Hill, Australia. Geochimica et Cosmochimica Acta, 69, 637–648.

Jiang, S.-Y., Yang, J.-H., Novák, M., and Selway, J. (2003) Chemical and boron isotopic compositions of tourmaline from the Lavicky leucogranite, Czech Republic. Geochemical Journal, 37, 545–556.

Jiang, S.-Y., Yu, J.-M., and Lu, J.-J. (2004) Trace and rare-earth element geochemistry in tourmaline and cassiterite from the Yunlong tin deposit, Yunnan, China: implication for migmatitic–hydrothermal fluid evolution and ore genesis. Chemical Geology, 209, 193–213.

Keays, R.R., and Jowitt, S.M. (2013) The Avebury Ni deposit, Tasmania: A case study of an unconventional nickel deposit. Ore Geology Reviews, 52, 4–17.

Klominsky, J. (1972) The Heemskirk granite massif, Western Tasmania, 285 p. Ph.D. thesis, University of Tasmania, Hobart.

Large, R.R. (1992) Australian volcanic-hosted massive sulfide deposits: features, styles, and genetic models. Economic Geology, 87, 471–510.

Le Fort, P. (1991) Enclaves of the Miocene Himalayan leucogranites. In J. Didier, and B. Barbarin, Eds., Enclaves and Granite Petrology, Developments in Petrology 13, p. 35–46. Elsevier, Amsterdam.

Leaman, D.E., and Richardson, R.G. (2003) A geophysical model of the major Tasmanian granitoids. Mineral Resources Tasmania, Tasmanian Geological Survey Record 2003/11, 1–8.

London, D. (1999) Stability of tourmaline in peraluminous granite systems: the boron cycle from anatexis to hydrothermal aureoles. European Journal of Mineralogy, 11, 253–262.

London, D., and Manning, D.A.C. (1995) Chemical variation and significance of tourmaline from Southwest England. Economic Geology, 90, 495–519.

London, D., Morgan VI, G.B., and Wolf, M.B. (1996) Boron in granitic rocks and their contact aureoles. In L.M. Anovitz, and E.S. Grew, Eds., Boron: Mineralogy, petrology and geochemistry, 33, p. 299–330. Reviews in Mineralogy and Geochemistry, Mineralogical Society of America, Chantilly, Virginia.

Marks, M.A.W., Marschall, H.R., Schühle, P., Guth, A., Wenzel, T., Jacob, D.E., Barth, M., and Gregor, M. (2013) Trace element systematics of tourmaline in pegmatitic and hydrothermal systems from the Variscan Schwarzwald (Germany): The importance of major element composition, sector zoning, and fluid or melt composition. Chemical Geology, 344, 73–90.

McClenaghan, M.P. (2006) The geochemistry of Tasmanian Devonian-Carboniferous granites and implications for the composition of their source rocks. Mineral Resources Tasmania, Tasmanian Geological Survey Record 2006/06, 1–31.

McDonough, W.F., Sun, S.-S., Ringwood, A.E., Jagoutz, E., Hofmann, A.W. (1992) Potassium, rubidium, and cesium in the Earth and Moon and the evolution of the mantle of the Earth. Geochimica et Cosmochimica Acta, 56, 1001–1012.

Morgan VI, G.B. (2016) A spreadsheet for calculating normative mole fractions of end-member species for Na-Ca-Li-Fe^{2+}-Mg-Al tourmalines from electron microprobe data. American Mineralogist, 101, 111–119.

Perugini, D., and Poli, G. (2007) Tourmaline nodules from Capo Bianco aplite (Elba Island, Italy): an example of diffusion limited aggregation growth in a magmatic system. Contributions to Mineralogy and Petrology, 153, 493–508.

Purvis, J.G. (1989) Tasmanian tin prospects part 1: West Tasmania Tin Province. Tasmanian Geological Survey Bulletin, p. 51–64.

Roda-Robles, E., Simmons, W., Pesquera, A., Gil-Crespo, P.P., Nizamoff, J., and Torres-Ruiz, J. (2015) Tourmaline as a petrogenic monitor of the origin and evolution of the Berry-Havey pegmatite (Maine, U.S.A.). American Mineralogist, 100, 95–109.

Rozendaal, A., and Bruwer, L. (1995) Tourmaline nodules: indicators of hydrothermal alteration and Sn-Zn-(W) mineralization in the Cape Granite Suite, South Africa. Journal of African Earth Sciences, 21, 141–155.

Samson, I.M., and Sinclair, W.D. (1992) Magmatic hydrothermal fluids and the origin of quartz-tourmaline orbicules in the Seagull Batholoth, Yukon Tertitory. The Canadian Mineralogist, 30, 937–954.

Sawka, W.N., Heizler, M.T., Kistler, R.W., and Chappell, B.W. (1990) Geochemistry of highly fractionated I- and S-type granites from the tin-tungsten province of western Tasmania. Geological Society of America, Special Paper 246, 161–180.

Scaillet, B., Pichavant, M., and Roux, J. (1995) Experimental crystallization of leucogranite magmas. Journal of Petrology, 36, 663–705.

Seedorff, E., Dilles, J.H., Proffett, J.M., Jr., Einaudi, M.T., Zurcher, L., Stavast, W.J.A., Johnson, D.A., and Barton, M.D. (2005) Porphyry deposits: Characteristics and origin of hydrogen features. Economic Geology 100th Anniversary Volume, 251–298.

Seymour, D.B., Green, G.R. and Calver, C.R. (2007) The geological and mineral deposits of Tasmania: a summary. Tasmanian Geological Survey Bulletin, 72, 1–29.

Shannon, J.R., Walker, B.M., Carten, R.B., and Geraghty, E.P. (1982) Unidirectional solidification textures and their significance in determining relative ages of intrusions at the Henderson Mine, Colorado. Geology, 10, 293–297.

Shewfelt, D. (2005) The nature and origin of Western Australian tourmaline nodules: A petrological, geochemical and isotopic study, 146 p. M.Sc. thesis, University of Saskatchewan.

Shinohara, H., and Kazahaya, K. (1995) Degassing processes related to magma-chamber crystallization. In J.F.H. Thompson, Ed., Magmas, fluids, and ore deposits, p. 47–70. Mineralogical Association of Canada Short Course 23.

Sinclair, W.D., and Richardson, J.M. (1992) Quartz-tourmaline orbicules in the Seagull Batholith, Yukon Territory. The Canadian Mineralogist, 30, 923–935.

Solomon, M., and Groves, D.I. (2000) The geology and origin of Australia's mineral deposits, 428–521 p. Centre for Ore Deposit Research, University of Tasmania, and Centre for Global Metallogeny, University of Western Australia.

Sun, S.-S., and McDonough, W.F. (1989) Chemical and isotopic systematics of oceanic basalts: implications for mantle composition and processes. Geological Society, London, 42, 313–345.

Trumbull, R.B., Krienitz, M.S., Gottesmann, B., and Wiedenbeck, M. (2008) Chemical and boron-isotope variations in tourmalines from an S-type granite and its source rocks: the Erongo granite and tourmalinites in the Damara Belt, Namibia. Contributions to Mineralogy and Petrology, 155, 1–18.

van Hinsberg, V.J. (2011) Preliminary experimental data on trace-element partitioning between tourmaline and silicate melt. The Canadian Mineralogist, 49, 153–163.

van Hinsberg, V.J., Henry, D.J., and Dutrow, B.L. (2011a) Tourmaline as a petrologic forensic mineral: A unique recorder of its geologic past. Elements, 7, 327–332.

van Hinsberg, V.J., Henry, D.J., and Marschall, H.R. (2011b) Tourmaline: an ideal indicator of its host environment. The Canadian Mineralogist, 49, 1–16.

van Hinsberg, V.J., Schumacher, J.C., Kearns, S., Mason, P.R.D., and Franz, G. (2006) Hourglass sector zoning in metamorphic tourmaline and resultant major and trace-element fractionation. American Mineralogist, 91, 717–728.

Veksler, I.V., and Thomas, R. (2002) An experimental study of B-, P- and F-rich synthetic granite pegmatite at 0.1 and 0.2 GPa. Contributions to Mineralogy and Petrology, 143, 673–683.

Veksler, I.V. (2004) Liquid immiscibility and its role at the magmatic-hydrothermal transition: a summary of experimental studies. Chemical Geology, 210, 7–31.

Waterhouse, L.L. (1916) The South Heemskirk Tinfield, 21 p. Tasmanian Geological Survey Bulletin, No. 21, 1–450.

Wilkinson, J.J., Chang, Z., Cooke, D.R., Baker, M.J., Wilkinson, C.C., Inglis, S., Chen H., and Gemmell, J.B. (2015) The chlorite proximitor: A new tool for detecting porphyry ore deposits. Journal of Geochemical Exploration, 152, 10–26.

Wolf, M.B., and London, D. (1997) Boron in granitic magmas: stability of tourmaline in equilibrium with biotite and cordierite. Contributions to Mineralogy and Petrology, 130, 12–30.

Yavuz, F., Jiang, S.-Y., Karakaya, N., Karakaya, M.Ç., and Yavuz, R. (2011) Trace-element, rare-earth element and boron isotopic compositions of tourmaline from a vein-type Pb–Zn–Cu ± U deposit, NE Turkey. International Geology Review, 53, 1–24.

Figure captures:

FIGURE 1. Simplified geological map showing rock sequences in northwest Tasmania and major granite-associated Sn-W deposits (after Solomon and Groves 2000). The Heemskirk and Pieman Heads granites crop out on the western Tasmanian coastline.

FIGURE 2. (a) Geological map showing principal feature of the Heemskirk Batholith and associated Sn-W deposits (modified from Klominsky 1972; Hajitaheri 1985). (b) Simplified cross-section A-A′ describing the geological outcrop at Trial Harbor, southern edge of the Heemskirk Batholith, where tourmaline-rich features, USTs, and biotite banding occur around the contact between the white and the red granites. (c) Sketched cross-section showing relative spatial distributions of tourmaline patches, orbicules, cavities, and veins that are hosted in the white granite.

FIGURE 3. Photographs showing textural and mineralogical features of tourmaline-rich features developed in the Heemskirk and Pieman Heads granites. (a) Tourmaline orbicules hosted in the equigranular white phase of the Heemskirk Granite at Trial Harbor. (b) Clusters of tourmaline orbicules beneath the quartz-rich USTs in the white granite. (c) A spherical 8 cm-diameter tourmaline orbicule consisting of inner and outer zones. (d) Subvertically oriented tourmaline orbicule-bearing aplitic dyke which fed the aplitic sill has cut across the equigranular white granite. (e) A subrounded tourmaline orbicule has been cut by a 1 cm-wide tourmaline vein in aplitic white granite. (f) An identical tourmaline-filled cavity has typical crystal zones, and is rimmed by quartz in the white Heemskirk Granite. (g) Clusters tourmaline orbicules occurring in the Pieman Heads Granite. (h) A tourmaline orbicule composing of coarse-grained quartz-tourmaline intergrowths, surrounded by a red-brown leucocratic K-feldspar and quartz. Abbreviation: Qz = quartz, Tur = tourmaline. Sample location: the Heemskirk Granite at Trial Harbor, E145°09′23.93″, S41°55′20.64″ ; the Pieman Heads Granite, E144°55′40.01″, S41°43′15.00″, Elevation = 3 to 30 m.

FIGURE 4. Photomicrographs showing mineralogical features of tourmaline-rich features developed in the Heemskirk Granite. Tourmaline patches: (a) euhedral plagioclase with polysynthetic twins in massive tourmaline and quartz, (b) residual K-feldspar in tourmaline has a jagged contact. Tourmaline orbicules: (c) tourmaline displays different pleochroism and textures between the inner and outer zones, (d) in the inner zone, sub- and euhedral quartz occur in a mosaic of greenish to blue pleochroic tourmaline. Tourmaline cavities: (e) prismatic tourmaline intergrown with quartz on the edge of a tourmaline cavity; irregular tourmaline grains have different pleochroism, and are interstitial to quartz, (f) massive tourmaline crystals displaying orange-brown to blue pleochroism, and greenish zones associated with sub-euhedral quartz grains. Tourmaline veins: (g) euhedral elongated tourmaline grains occur in the central zone of the veins, selvaged by quartz-muscovite halo, (h) quartz-muscovite alteration halo comprising of granular quartz partly embayed and pre-existing feldspar totally replaced by muscovite. All the photomicrographs taken under cross polarized light, except (e) under plane polarized light. Abbreviation: Kfs = K-feldspar, Pl = plagioclase, Qz = quartz, Ms = muscovite, Tur = tourmaline. Sample location: E145°09′23.93″, S41°55′20.64″, Elevation = 3 to 30 m.

FIGURE 5. (a) Primordial mantle-normalized multi-element spider plots (values from McDonough et al. 1992), (b) chondrite-normalized rare earth element plots (values from Sun and McDonough 1989) for the Heemskirk and Pieman Heads granites, as well as tourmaline orbicules from western Tasmania. GH = Granville Harbor, TH = Trial Harbor, PH = Pieman Heads, Tur = tourmaline

FIGURE 6. Representative BSE images showing the distinct growth zonation of tourmaline from the western Tasmanian granites. Oscillatory zoning is commonly identified in tourmalines in cavities (a and b, Sample

WT12WH35) from Granville Harbor, Heemskirk Batholith, and tourmalines in veins (c and d, Sample WT12WH13-1) from the Pieman Heads Granite. Concentric zoning is typically discerned in tourmalines from orbicules (e, Sample WT12WH28-3) at Trial Harbor, Heemskirk Batholith, from veins (f, Sample WT12WH13-1) from the Pieman Heads Granite, and from patches (g, Sample WT12WH20) at Trial Harbor. Radial zoning is mainly observed in tourmaline hosted in orbicules (h and i, Sample WT12WH28-4) from Trial Harbor. Most grains are sectioned in a plane perpendicular or parallel to the c-axis, except for the tourmaline grain (b, h, and i) oblique to the c-axis.

FIGURE 7. Selected binary plots showing the compositional variations of tourmalines from the Heemskirk Batholith (a and b), and from the Pieman Heads Granite (c and d). $^{X}\square$ represents the proportions of vacancies at X-site. Tur = tourmaline, apfu = atom per formula.

FIGURE 8. Binary plots showing exchange vectors and compositional variations in tourmalines from the Heemskirk Batholith (a and c), and from the Pieman Heads granite (b and d). R^{2+} = Fe + Mg + Mn, and Fe is dominant in R^{2+}. Tur = tourmaline, apfu = atom per formula.

FIGURE 9. ^{Y}Al versus Mn plot shows the extremely Mn- and Al-rich tourmalines from veins associated within the Pieman Heads Granite. Symbols are same as those in Figure 8. Tur = tourmaline, apfu = atom per formula.

FIGURE 10. Percentile box and whisker plots showing comparisons of representative trace elements in tourmalines and host granites from western Tasmania. Tourmalines and whole rocks were analyzed by LA-ICP-MS and ICP-ES/ICP-MS, respectively. Analytical numbers of each group are annotated in the brackets. Tur = tourmaline, WR = whole rock, TH = Heemskirk Granite at Trial Harbor, GH = Heemskirk Granite at Granville Harbor, PH = Pieman Heads Granite.

FIGURE 11. Comparisons of whole-rock, tourmaline orbicule and tourmaline LA-ICP-MS geochemical data, showing mean, median, 25th and 75th percentile results. (a) Elements that are preferentially incorporated in tourmaline. (b) Elements that are relatively depleted in tourmaline relative to the host granites. WR = whole rock, TOs = tourmaline orbicules, Tur = tourmaline.

FIGURE 12. Representative combined EMPA and LA-ICP-MS profiles show chemical variations across the sectors of tourmalines from Trial Harbor (a, tourmaline patch; b, tourmaline cavity), Heemskirk Batholith, and the Pieman Heads Granite (c and d, tourmaline veins). Major and trace elements are obtained by EMPA and LA-ICP-MS, respectively. Corresponding analyzed numbers and sites are marked in the BSE images. Tourmaline grains were sectioned approximately perpendicular to the c-axis, except grain (d) which was cut parallel to the c-axis. The shaded areas in chemical plots represent the sector of the grain.

FIGURE 13. Al-Fe-Mg ternary diagram showing tourmalines from various source rocks (modified from Henry and Guidotti 1985). Note that tourmalines from the Heemskirk and Pieman Heads granites are plotted mostly into the Li-poor granitoid field, and minor into the Li-rich granitoid field.

FIGURE 14. Plots of major elements versus selective trace elements for tourmalines from western Tasmanian granites. Major and trace elements in tourmalines were analyzed by EMPA and LA-ICP-MS, respectively. Fe/(Fe+Mg) ratios correlate inversely with transition elements (a, b, and c) and Sr (e), but positively with Be (d) and high field strength elements (f). Na/(Na+$^{X}\square$) ratios appear to have a positive correlation with Pb (g), REE (h), and Nb (i). Tur = tourmaline, apfu = atom per formula.

FIGURE 15. Idealized scenarios showing the formation of tourmaline-rich features in the western Tasmanian

granites. (a) S-type magmas which were formed by partial melting of metapelitic rocks emplace into the shallow crust. Due to continuous decompression and crystallization, a spanning cluster of volatile bubbles (enriched in B, Fe, Na etc.) separates from the aluminosilicate-rich melt (Candela 1991; Veksler 2004). (b) Buoyant boron-rich aqueous bubbles migrate upwards between grain boundaries in the manner of bubble-laden plumes at low degrees of crystallization (Candela 1991). Tourmaline patches are explained to be the remnants of the bubble-laden plumes which ultimately collapse due to diminishment of the volatile supply. (c) At high degrees of crystallization, the boron-rich bubbles are likely to be trapped into pockets of peripheral magma because capillary forces can drive abundant water and volatiles adhering to the crystal mush of alumino-siliceous components (Shinohara and Kazahaya 1995). These buoyant bubbles may gradually percolate through a crystal mush and coalesce to become larger. Tourmaline orbicules and cavities are interpreted to the relicts of these entrapped bubble phases when the magma cools down. (d) At the final stage of granite crystallization and emplacement, the accumulating vapor pressure exceeds the lithostatic load, leading to the fracture failure of the granitic carapace and neighboring wallrocks. Boron-rich aqueous fluids migrate along these fractures, hydrothermally alter the host rocks, and eventually seal the fractures (Burnham 1979).

FIGURE 16. Discrimination plots showing trace element ratios versus Sn from whole-rock granite and tourmaline LA-ICP-MS data. (a) Zn/Nb versus Sn, (b) Co/Nb versus Sn, (c) Sr/Ta versus Sn, (d) Co/La versus Sn. The trace element ratios versus Sn in tourmaline can discriminate the well-mineralized Heemskirk Granite at Trial Harbor from the barren Pieman Heads Granite from western Tasmania.

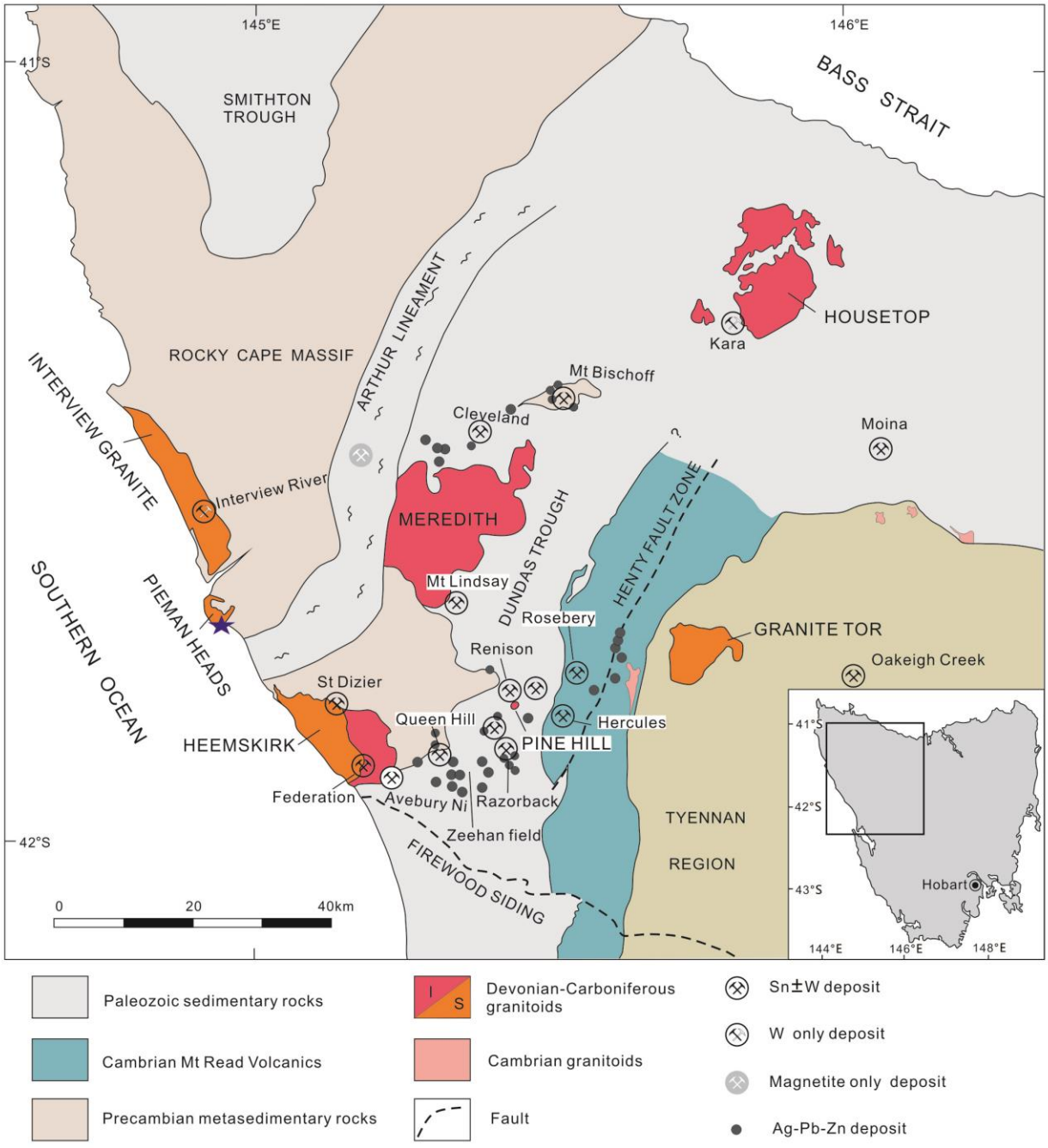
145°E
146°E
41°S
42°S
SMITHTON TROUGH
BASS STRAIT
ROCKY CAPE MASSIF
ARTHUR LINEAMENT
INTERVIEW GRANITE
Interview River
HOUSETOP
Kara
Mt Bischoff
Cleveland
Moina
MEREDITH
DUNDAS TROUGH
HENTY FAULT ZONE
Mt Lindsay
Rosebery
GRANITE TOR
Oakeigh Creek
Renison
St Dizier
Queen Hill
Hercules
PINE HILL
HEEMSKIRK
Federation
Avebury Ni
Razorback
Zeehan field
TYENNAN REGION
FIREWOOD SIDING
SOUTHERN OCEAN
PIEMAN HEADS
0
20
40km
43°S
Hobart
144°E
146°E
148°E
Paleozoic sedimentary rocks
Cambrian Mt Read Volcanics
Precambian metasedimentary rocks
I
S
Devonian-Carboniferous granitoids
Cambrian granitoids
Fault
Sn±W deposit
W only deposit
Magnetite only deposit
Ag-Pb-Zn deposit

Figure 1.

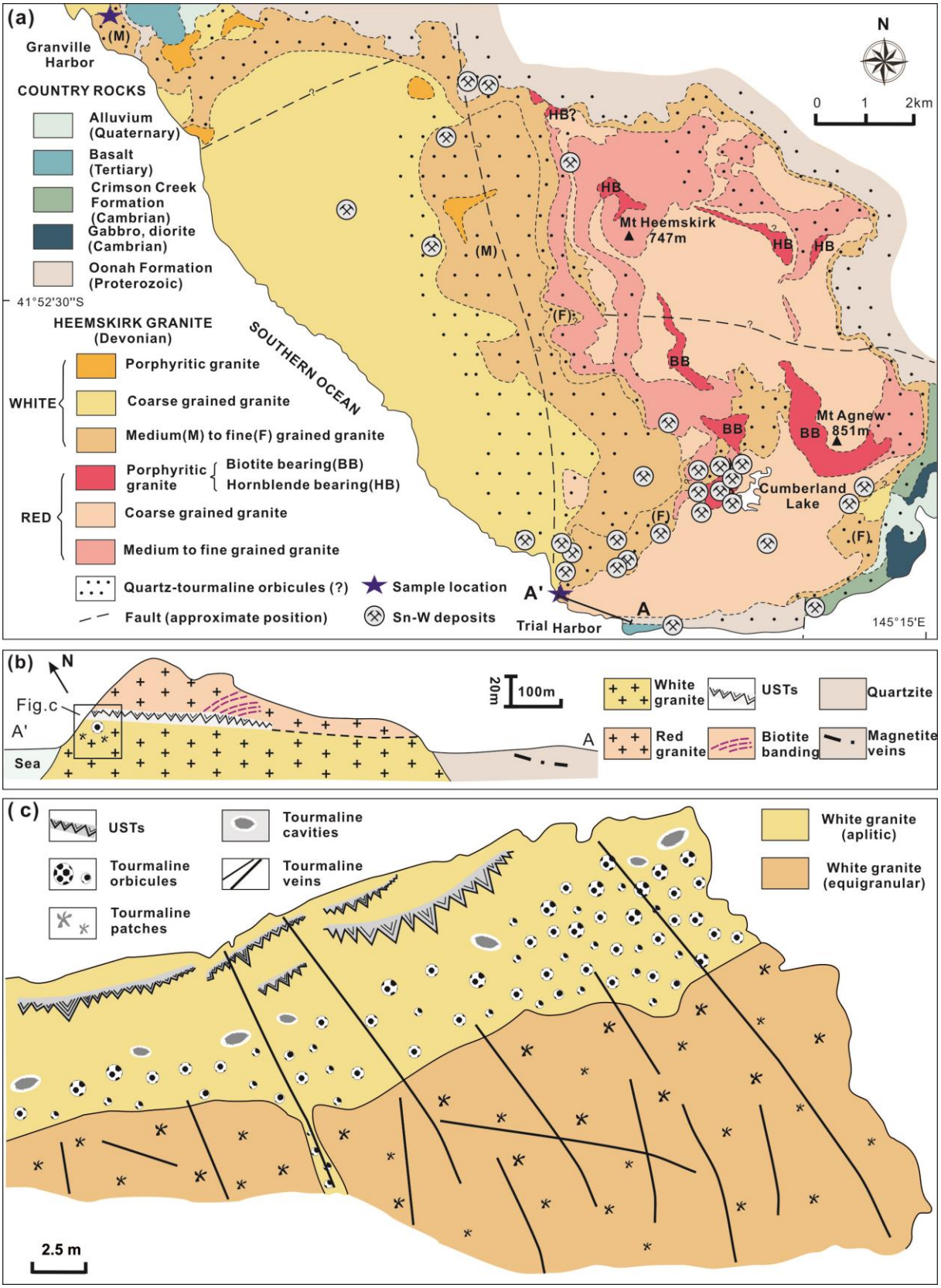
(a)
Granville Harbor
(M)
COUNTRY ROCKS
Alluvium (Quaternary)
Basalt (Tertiary)
Crimson Creek Formation (Cambrian)
Gabbro, diorite (Cambrian)
Oonah Formation (Proterozoic)
41°52'30"S
HEEMSKIRK GRANITE (Devonian)
WHITE
Porphyritic granite
Coarse grained granite
Medium(M) to fine(F) grained granite
RED
Porphyritic granite
Biotite bearing(BB)
Hornblende bearing(HB)
Coarse grained granite
Medium to fine grained granite
Quartz-tourmaline orbicules (?)
Sample location
Fault (approximate position)
Sn-W deposits
SOUTHERN OCEAN
HB?
HB
Mt Heemskirk 747m
(M)
(F)
BB
Mt Agnew 851m
Cumberland Lake
A'
A
Trial Harbor
145°15'E
N
0 1 2km
(b)
N
Fig.c
A'
Sea
20m
100m
A
White granite
USTs
Quartzite
Red granite
Biotite banding
Magnetite veins
(c)
USTs
Tourmaline orbicules
Tourmaline patches
Tourmaline cavities
Tourmaline veins
White granite (aplitic)
White granite (equigranular)
2.5 m

Figure 2.

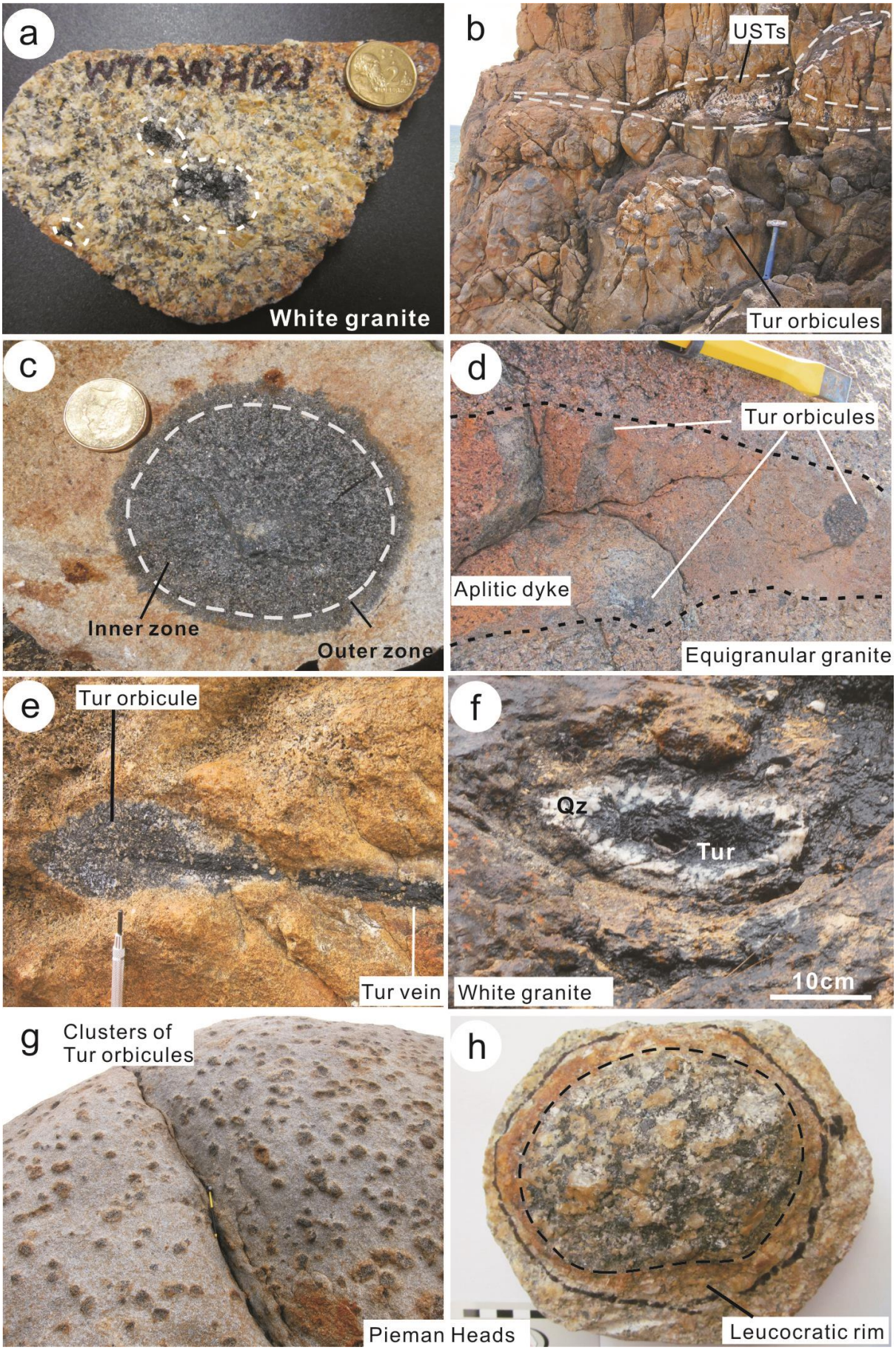
a
WT12WHD21
White granite
b
USTs
Tur orbicules
c
Inner zone
Outer zone
d
Tur orbicules
Aplitic dyke
Equigranular granite
e
Tur orbicule
Tur vein
f
Qz
Tur
White granite
10cm
g
Clusters of
Tur orbicules
Pieman Heads
h
Leucocratic rim

Figure 3.

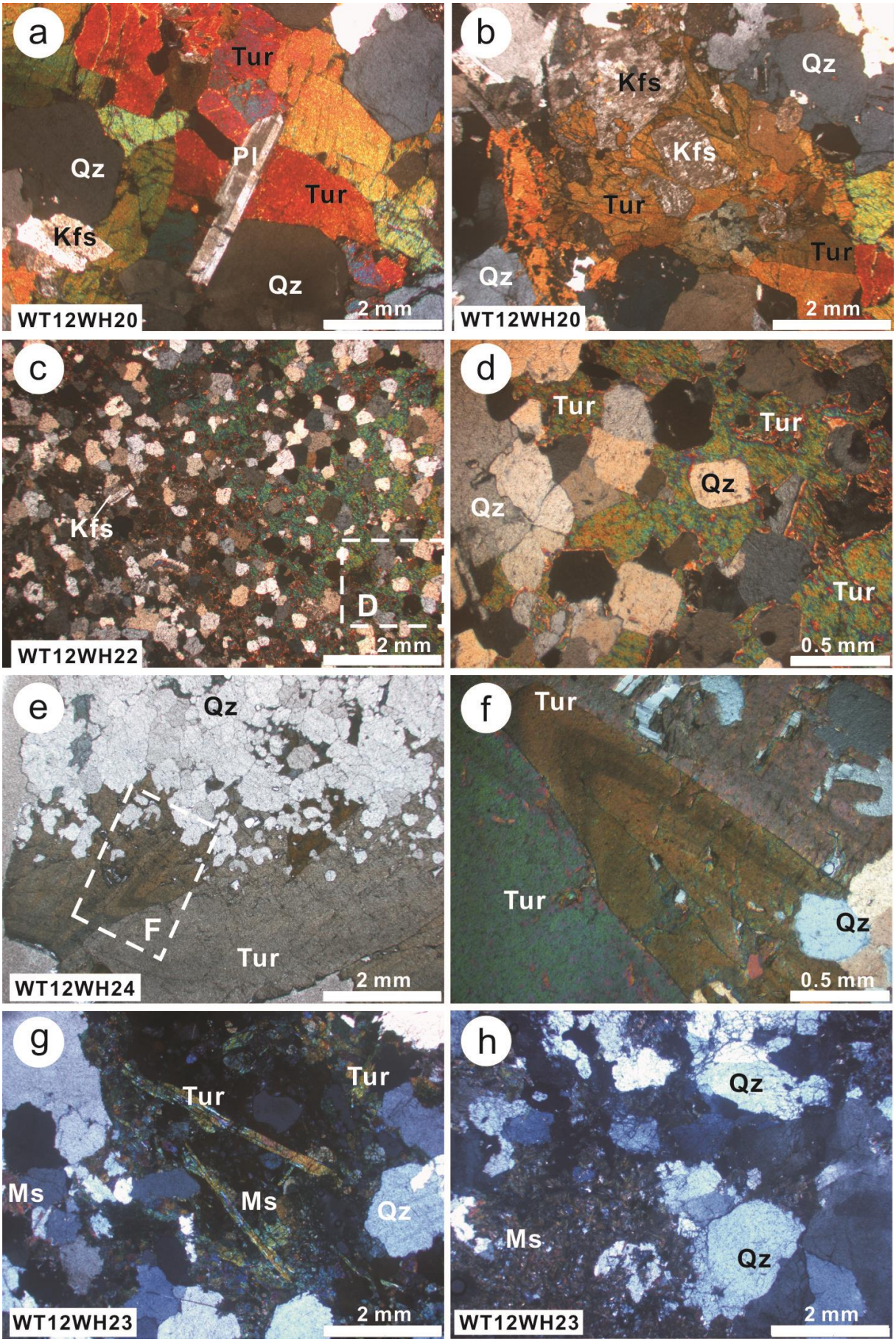
a
Tur
Pl
Qz
Tur
Kfs
Qz
2 mm
WT12WH20
b
Qz
Kfs
Kfs
Tur
Tur
Qz
2 mm
WT12WH20
c
Kfs
D
2 mm
WT12WH22
d
Tur
Tur
Qz
Qz
Tur
0.5 mm
e
Qz
F
Tur
2 mm
WT12WH24
f
Tur
Tur
Qz
0.5 mm
g
Tur
Tur
Ms
Ms
Qz
2 mm
WT12WH23
h
Qz
Ms
Qz
2 mm
WT12WH23

Figure 4.

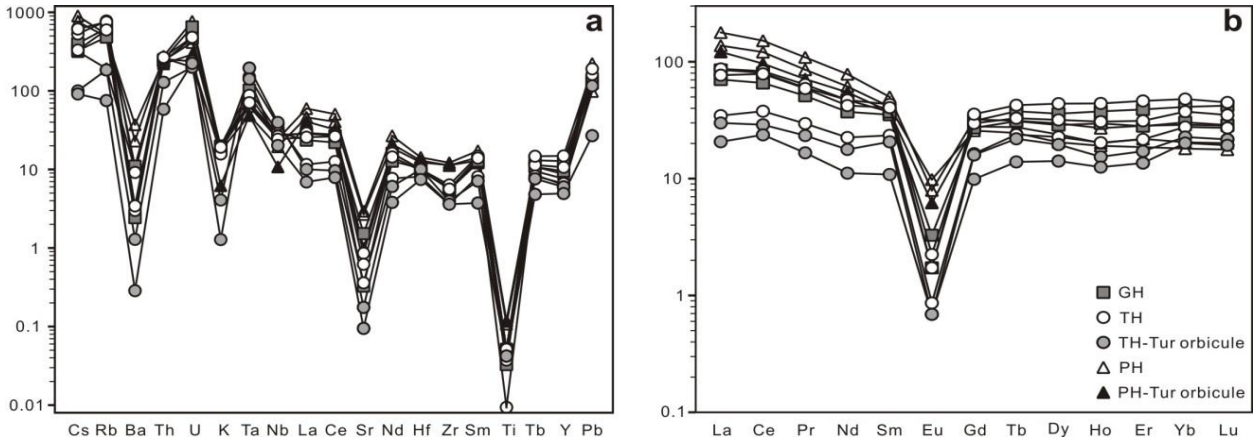

Figure 5.

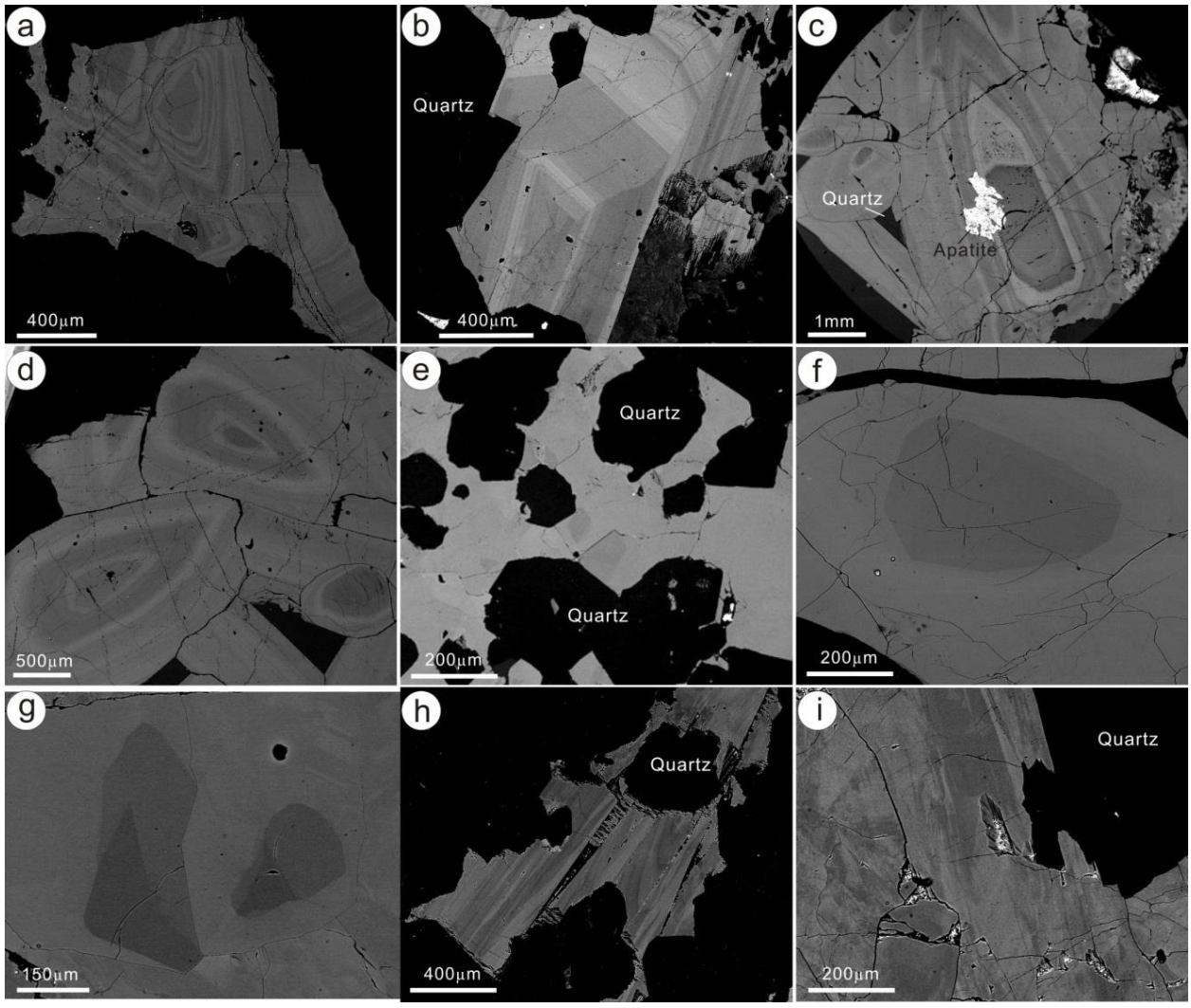

Figure 6.

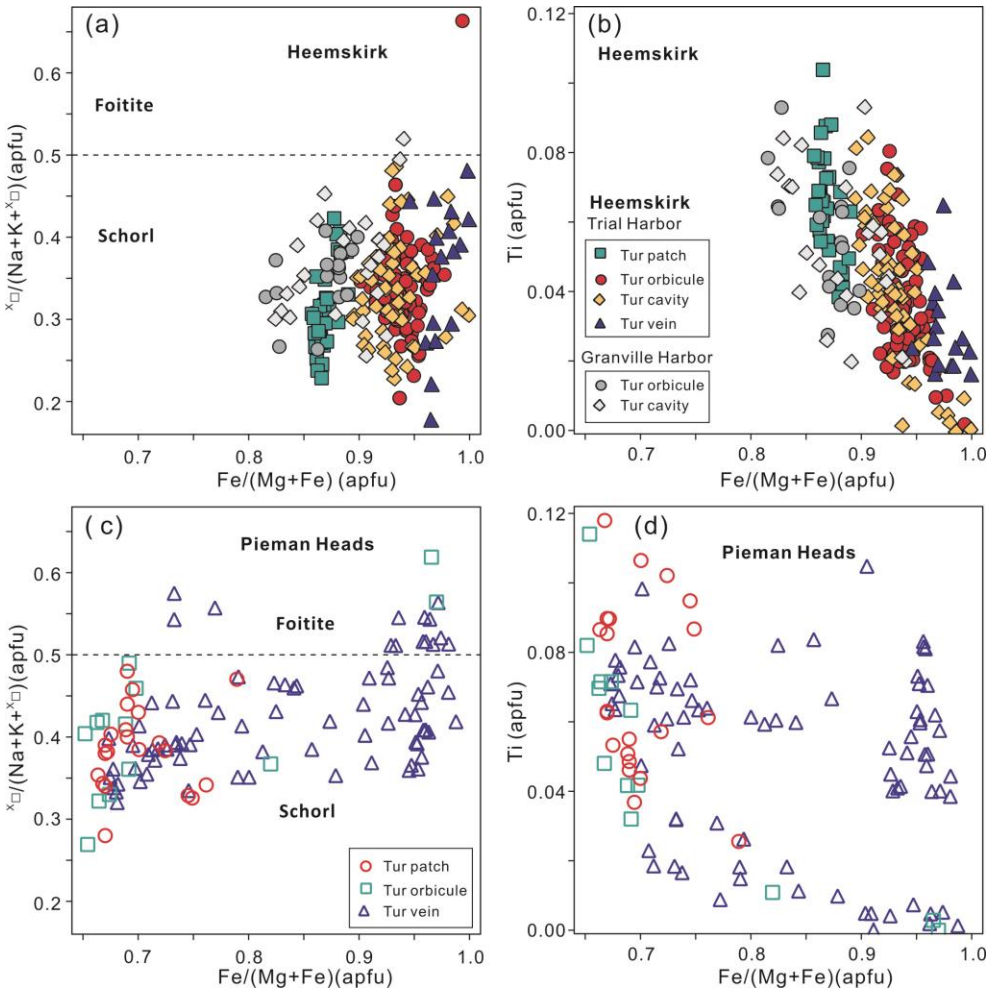

Figure 7.

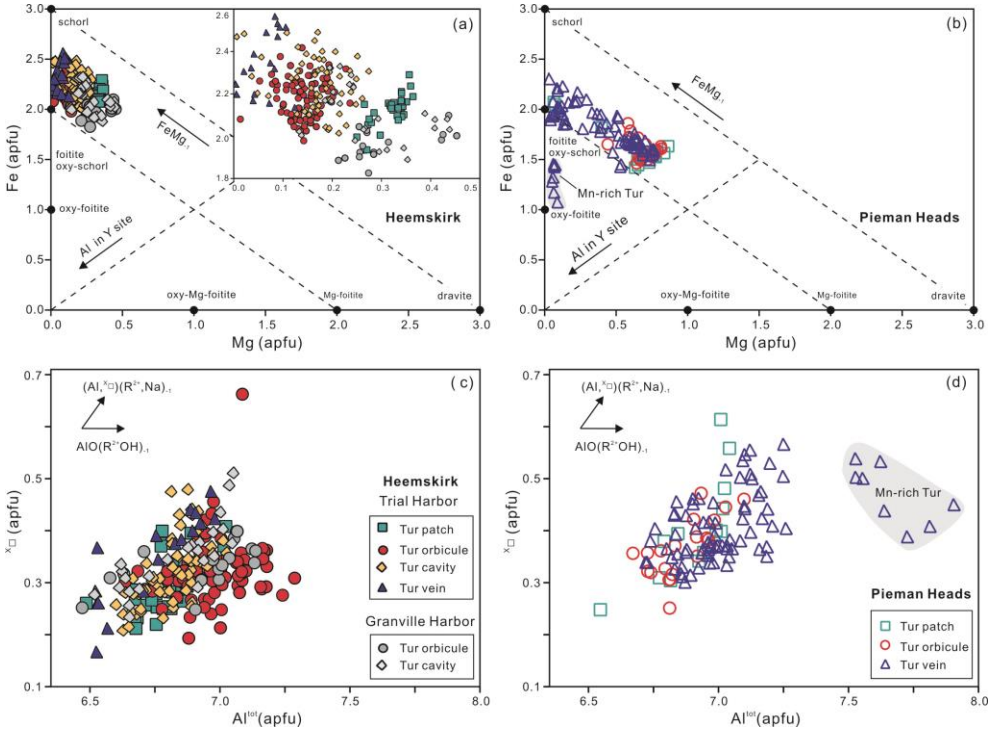

Figure 8.

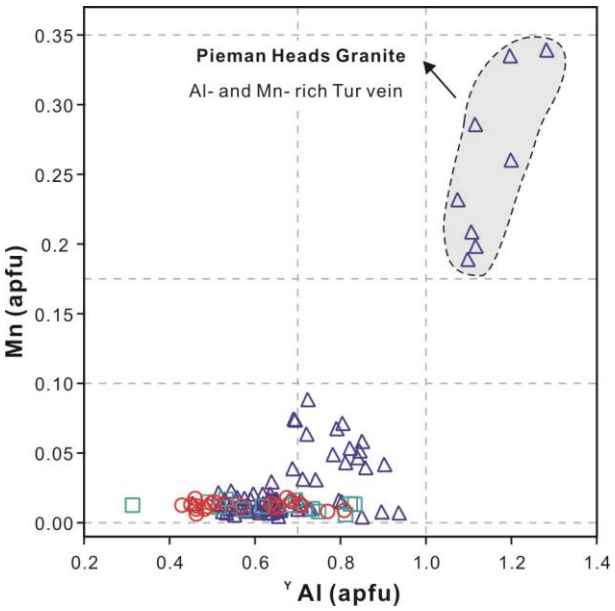
Pieman Heads Granite
Al- and Mn- rich Tur vein
Mn (apfu)
0.35
0.30
0.25
0.2
0.15
0.10
0.05
0.00
0.2
0.4
0.6
0.8
1.0
1.2
1.4
Y Al (apfu)

Figure 9.

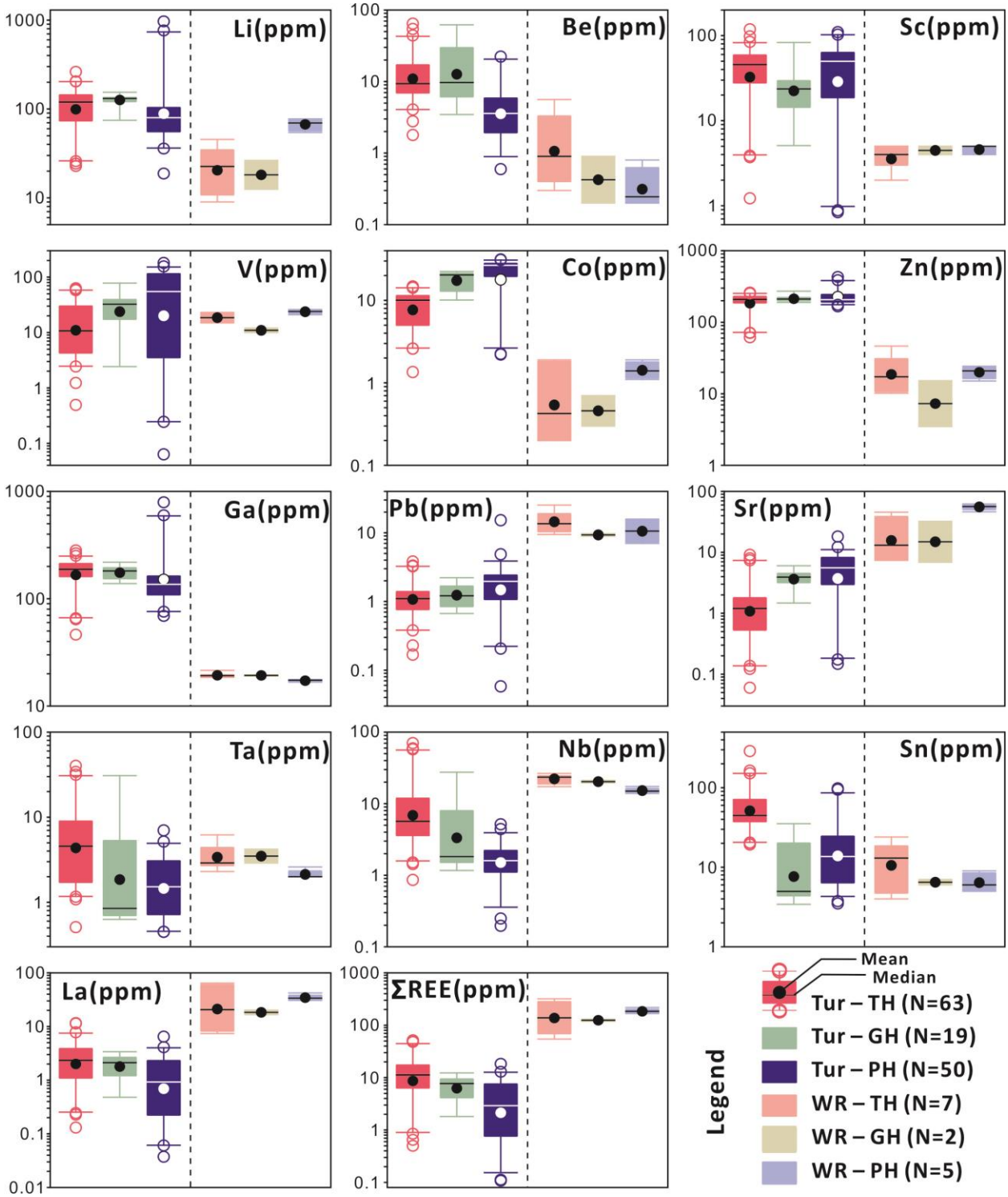
Li(ppm)
Be(ppm)
Sc(ppm)
V(ppm)
Co(ppm)
Zn(ppm)
Ga(ppm)
Pb(ppm)
Sr(ppm)
Ta(ppm)
Nb(ppm)
Sn(ppm)
La(ppm)
ΣREE(ppm)
Mean
Median
Legend
Tur – TH (N=63)
Tur – GH (N=19)
Tur – PH (N=50)
WR – TH (N=7)
WR – GH (N=2)
WR – PH (N=5)

Figure 10.

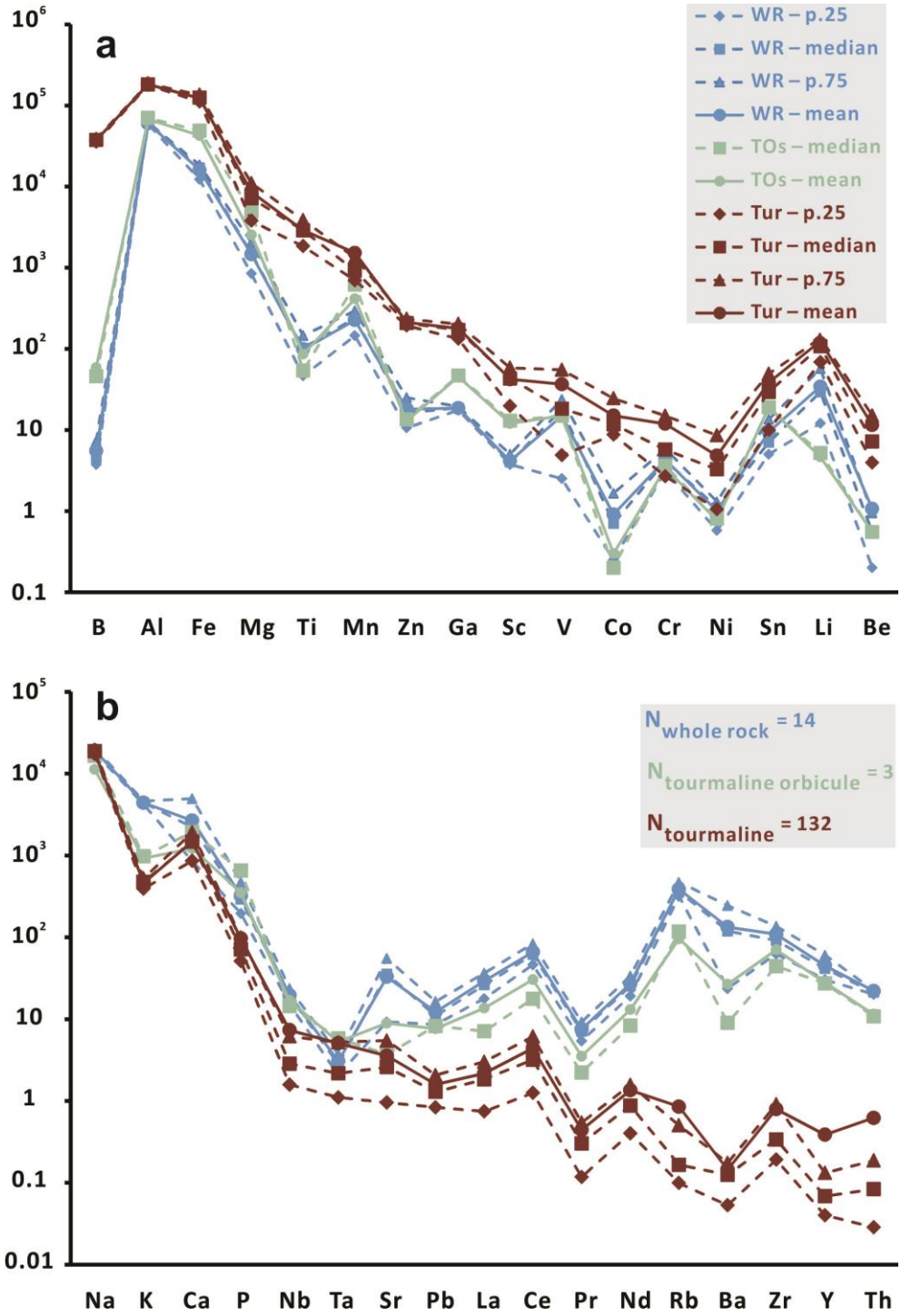
a
WR – p.25
WR – median
WR – p.75
WR – mean
TOs – median
TOs – mean
Tur – p.25
Tur – median
Tur – p.75
Tur – mean
10^6
10^5
10^4
10^3
10^2
10
1
0.1
B Al Fe Mg Ti Mn Zn Ga Sc V Co Cr Ni Sn Li Be
b
N whole rock = 14
N tourmaline orbicule = 3
N tourmaline = 132
10^5
10^4
10^3
10^2
10
1
0.1
0.01
Na K Ca P Nb Ta Sr Pb La Ce Pr Nd Rb Ba Zr Y Th
Figure 11.

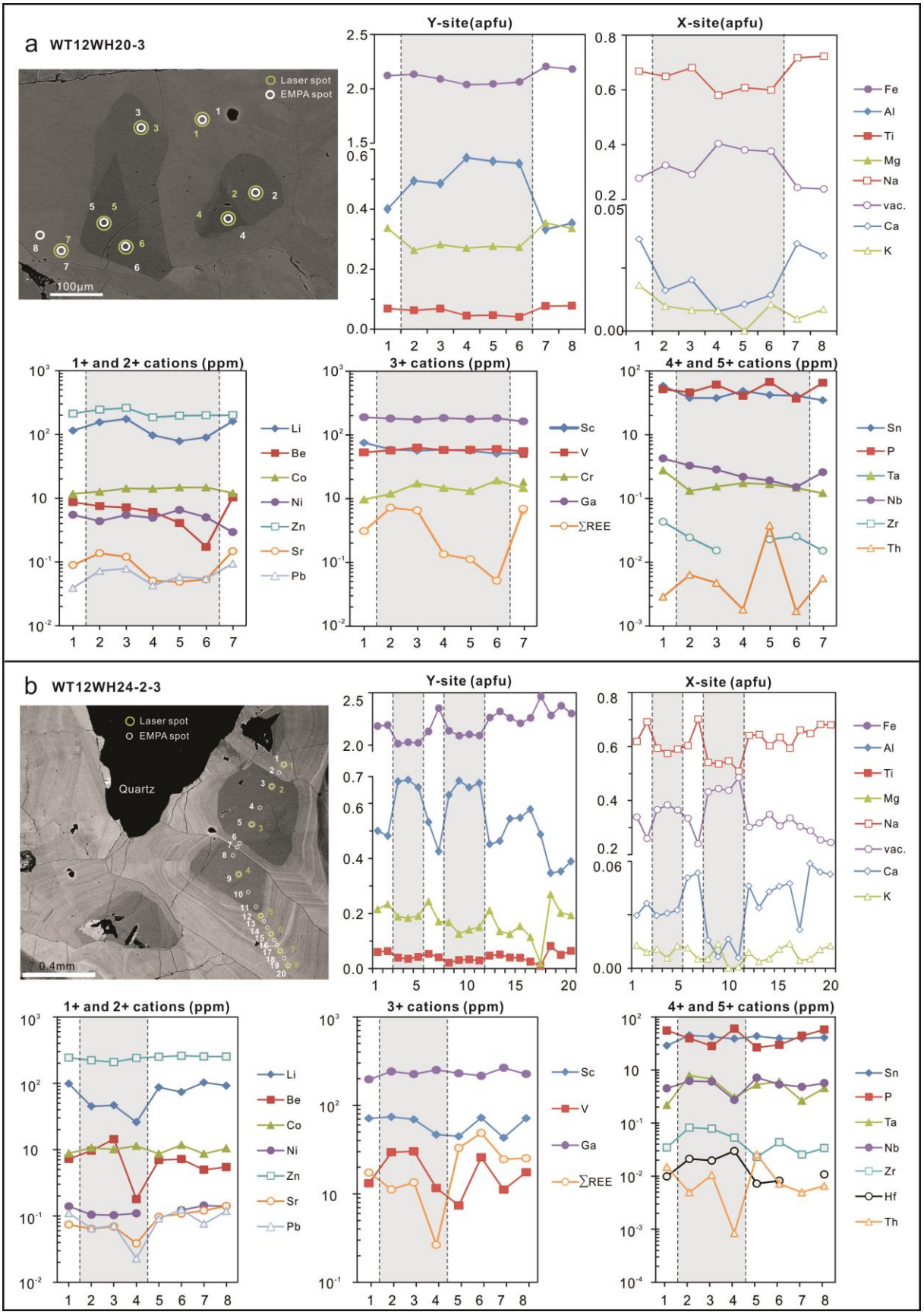
a WT12WH20-3
Laser spot
EMPA spot
100μm
Y-site(apfu)
X-site(apfu)
Fe
Al
Ti
Mg
Na
vac.
Ca
K
1+ and 2+ cations (ppm)
3+ cations (ppm)
4+ and 5+ cations (ppm)
Li
Be
Co
Ni
Zn
Sr
Pb
Sc
V
Cr
Ga
∑REE
Sn
P
Ta
Nb
Zr
Th
b WT12WH24-2-3
Laser spot
EMPA spot
Quartz
0.4mm
Y-site (apfu)
X-site (apfu)
Fe
Al
Ti
Mg
Na
vac.
Ca
K
1+ and 2+ cations (ppm)
3+ cations (ppm)
4+ and 5+ cations (ppm)
Li
Be
Co
Ni
Zn
Sr
Pb
Sc
V
Ga
∑REE
Sn
P
Ta
Nb
Zr
Hf
Th

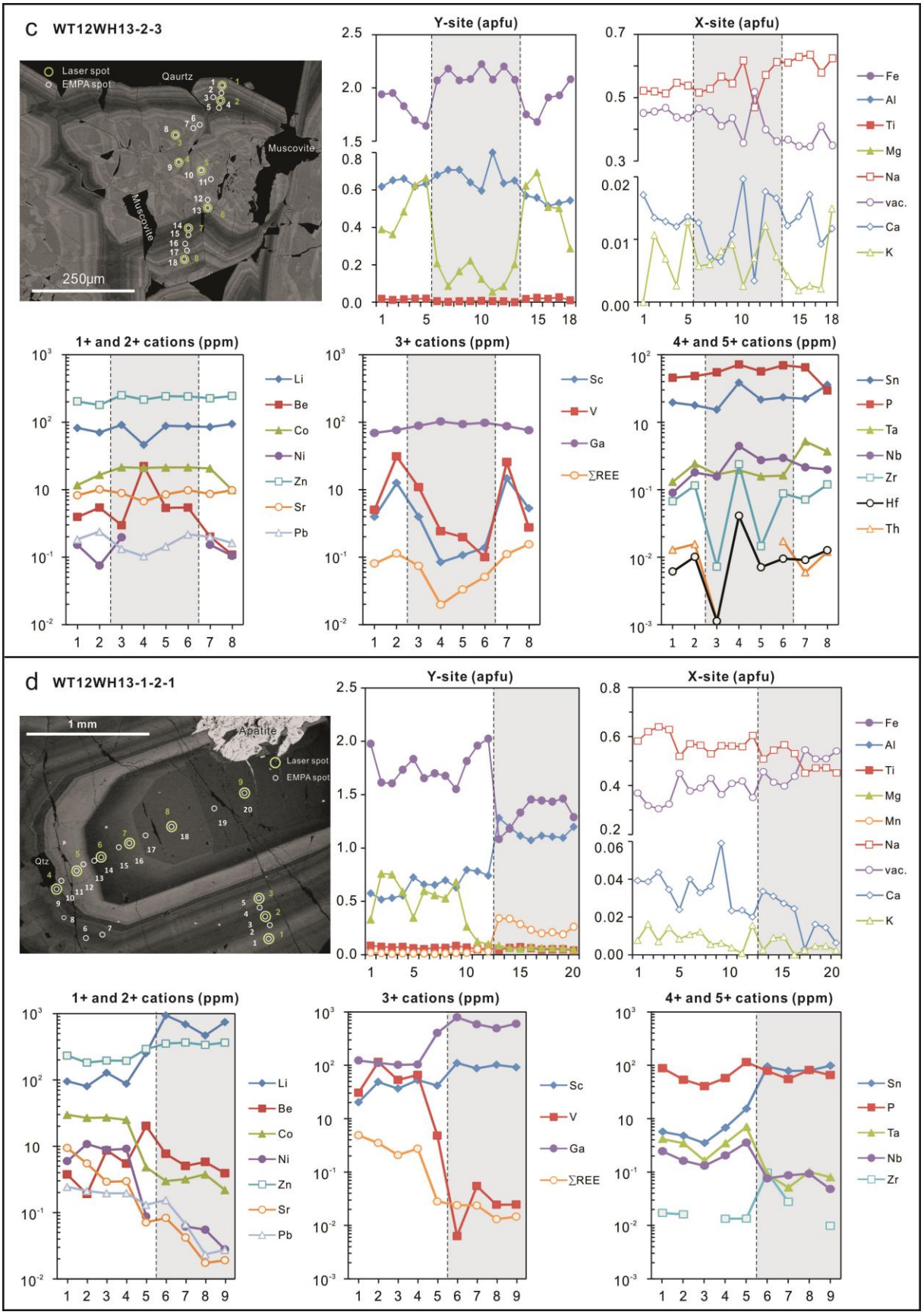
C WT12WH13-2-3
Laser spot
EMPA spot
Qaurtz
Muscovite
Muscovite
250μm
Y-site (apfu)
X-site (apfu)
Fe
Al
Ti
Mg
Na
vac.
Ca
K
1+ and 2+ cations (ppm)
3+ cations (ppm)
4+ and 5+ cations (ppm)
Li
Be
Co
Ni
Zn
Sr
Pb
Sc
V
Ga
∑REE
Sn
P
Ta
Nb
Zr
Hf
Th
d WT12WH13-1-2-1
1 mm
Apatite
Laser spot
EMPA spot
Qtz
Y-site (apfu)
X-site (apfu)
Mn
1+ and 2+ cations (ppm)
3+ cations (ppm)
4+ and 5+ cations (ppm)

Figure 12.

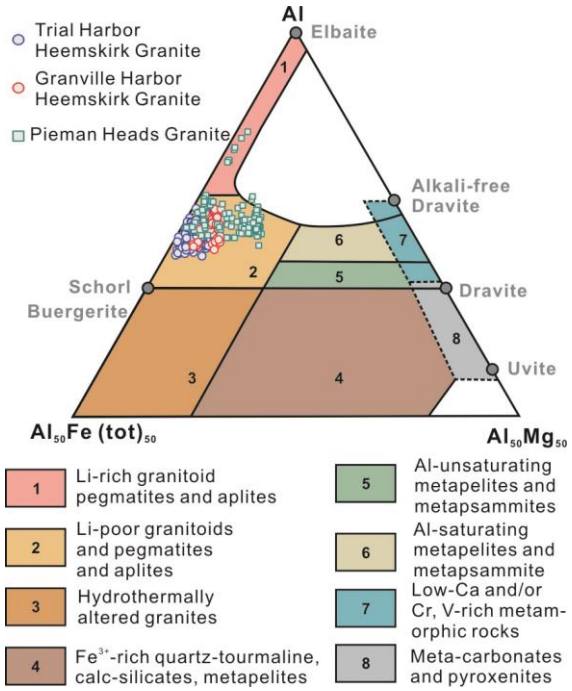

Figure 13.

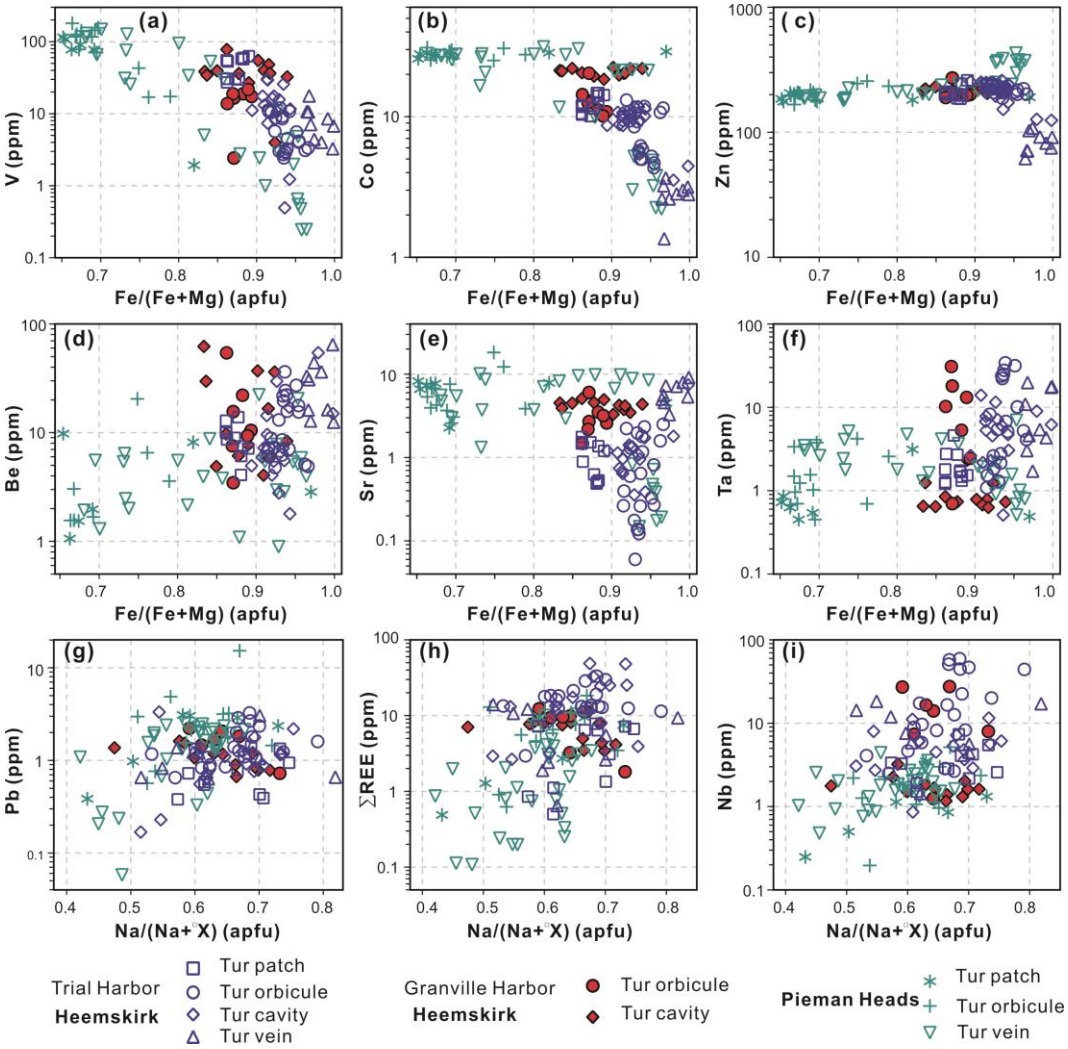

Figure 14.

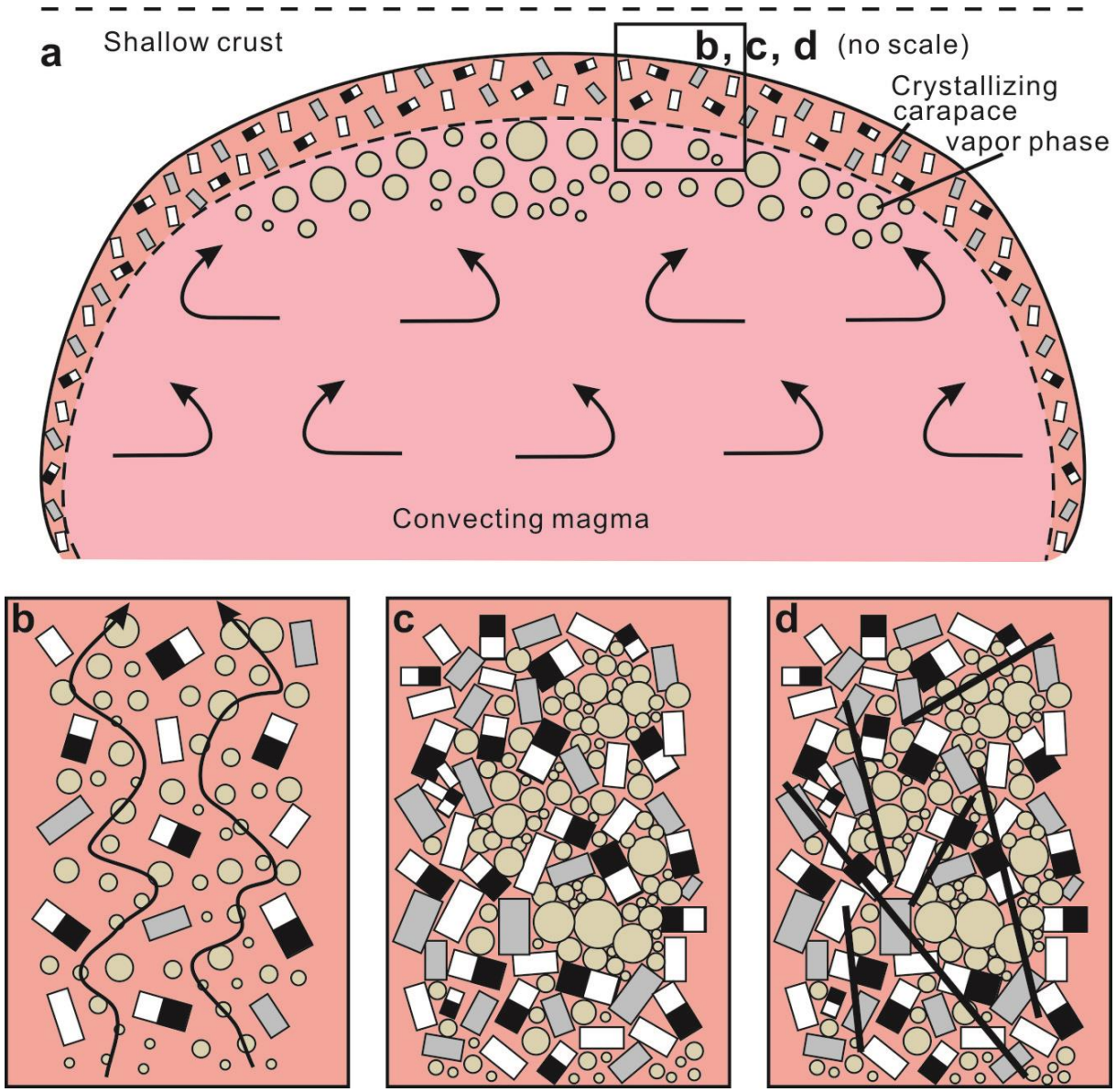
a
Shallow crust
b, c, d (no scale)
Crystallizing carapace
vapor phase
Convecting magma
b
c
d

Figure 15.

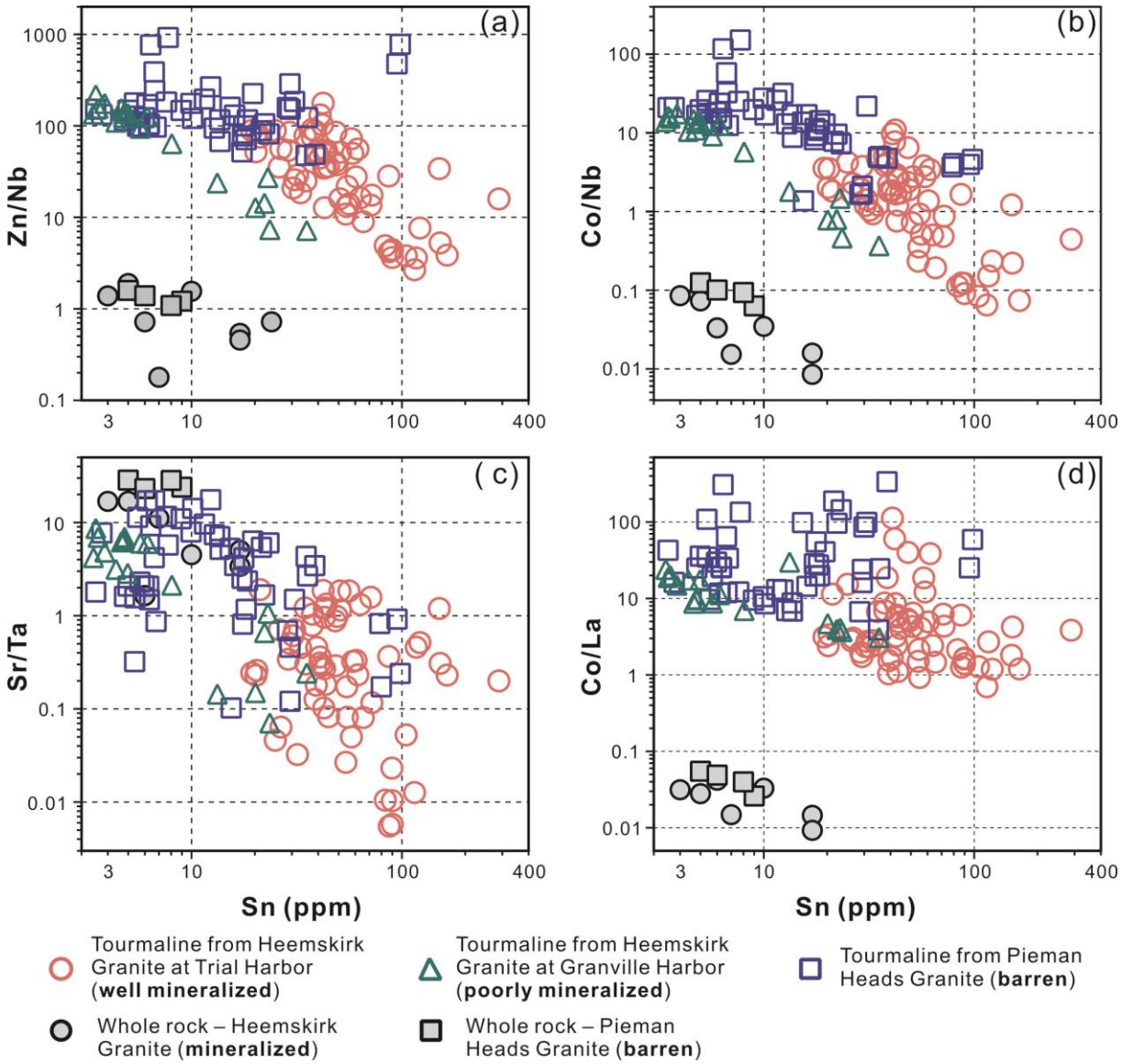
(a)
(b)
(c)
(d)
Zn/Nb
Co/Nb
Sr/Ta
Co/La
Sn (ppm)
Sn (ppm)
Tourmaline from Heemskirk Granite at Trial Harbor (well mineralized)
Tourmaline from Heemskirk Granite at Granville Harbor (poorly mineralized)
Tourmaline from Pieman Heads Granite (barren)
Whole rock – Heemskirk Granite (mineralized)
Whole rock – Pieman Heads Granite (barren)

Figure 16.

Tables:

TABLE 1. Sn, W, Fe and Ni deposits associated with the Heemskirk Granite, western Tasmania

Field	Deposit	Commodity	Tonnage (Mt)	Grade	Reference
South Heemskirk	Tenth Legion	Sn-Fe	0.9 6.0	0.4 - 0.5 % Sn 60 % Fe	Purvis 1989
	Colemans	Sn	0.5	0.2 % Sn	
	Sweeneys	Sn	0.5	0.6 % Sn	
	Federation Globe	Sn	> 1.5	0.5 - 0.6 % Sn	
	Avebury	Ni	29.3	0.9 % Ni	Keays and Jowitt 2013
North Heemskirk	St. Dizer	Sn-W-Fe	~2.6	0.5 % Sn 0.05 % WO_3	Seymour et al. 2007
Zeehan	Severn	Sn	4.17	0.98 % Sn	Callaghan 2013
	Montana	Sn	0.51	1.91 % Sn	
	Queen Hill	Sn	3.6	1.2 % Sn	Seymour et al. 2007
	Oonah	Sn	1.0	0.7- 1 % Sn	Purvis 1989

TABLE 2. Tourmaline- and quartz-rich textured features in the Heemskirk and Pieman Heads granites

Type	Granite locations	Host granite	Mineral association	Morphology	Distribution, mineral zone, alteration
Tourmaline patches	Heemskirk Granite at Trial and Granville Harbor, Pieman Heads Granite	Equigranular, locally porphyritic	Quartz, K-feldspar, plagioclase, tourmaline, biotite, muscovite, zircon, monazite, titanite, or apatite	Irregular, dendritic, 0.5-2 cm in diameter	Disseminated in the carapace of the host granites; no mineral zones; weak to moderate muscovite alteration; beneath the orbicule-rich aplitic and/or equigranular sill or UST layers; apatite only occurs at Granville Harbor and Pieman Heads Granite
Tourmaline orbicules	Heemskirk Granite at Trial and Granville Harbor, Pieman Heads Granite	Equigranular, locally porphyritic, and aplitic at Trial Harbor	Quartz, K-feldspar, plagioclase, tourmaline, muscovite, zircon, monazite, titanite, or apatite	Spherical, elliptic, 3-15 cm in diameter	Locally composing 15-20 % by volume of the local granitic cupolas; internal tourmaline-rich rimed by tourmaline-quartz intergrowths or K-feldspar-quartz; weak muscovite alteration; commonly occur in aplitic sills (~ 30 m thick) and also in orbicule-hosted aplitic feed dykes at Trial Harbor, or in the equigranular granite at Granville Harbor and Pieman Heads, locally in a higher granitic sill than the patches
Tourmaline cavities	Heemskirk Granite at Trial and Granville Harbor	Equigranular, locally porphyritic and aplitic	Quartz, tourmaline, muscovite, zircon, monazite, titanite	Spherical, subround, 2 cm up to 2 m ~~15 cm~~ in diameter	Typically having a central tourmaline-rich zone and a quartz-rich rim; develop intensive muscovite-quartz alteration halo; occur in high levels of the orbicule-rich equigranular and/or porphyritic granite, or aplitic sill at Trial Harbor
Tourmaline veins	Heemskirk Granite at Trial and Granville Harbor, Pieman Heads Granite		Quartz, tourmaline, muscovite, zircon, titanite, xenotime, or apatite	Discrete chains, several cm to m wide	Central tourmaline-quartz zone rimed by quartz and muscovite halo; intense muscovite-quartz alteration; occur in all exposed levels of the two granites, and have cut the orbicules, USTs and/or cavities locally; apatite only occurs in the Pieman Heads Granite
Unidirectional solidification textures (USTs)	Heemskirk Granite, particularly Trial and Granville Harbor	Equigranular and aplitic	Quartz, K-feldspar, plagioclase, biotite, tourmaline, muscovite, magnetite, chlorite, zircon, monazite, or rutile	Comb, crenulate layer; coarse-grained quartz up to 5 cm; locally hundreds of meters long	Occurring in higher sills than the tourmaline orbicules and/or cavities in the upper carapace of an intrusion; commonly alternating with aplitic layers; marking the boundary of the overlying red-phase and underlying white-phase granites; locally crosscut by tourmaline-quartz veins; experienced K-feldspar and/or muscovite alteration, and selective chlorite alteration around magnetite in the USTs at Granville Harbor

TABLE 3. Average major element compositions of tourmalines from the Heemskirk and Pieman Heads granites, analyzed by EMPA

Location	Trial Harbor, Heemskirk								Granville Harbor, Heemskirk				Pieman Heads Granite					
Feature	Patch (n=34)		Orbicule (n=85)		Cavity (n=57)		Vein (n=17)		Orbicule (n=16)		Cavity (n=24)		Patch (n=13)		Orbicule (n=21)		Vein (n=80)	
	Av.	SD	Av.	SD	Av.	SD	Av.	SD	Av.	SD	Av.	SD	Av.	SD	Av.	SD	Av.	SD
SiO_2 wt%	33.07	0.38	32.87	0.52	33.03	0.48	33.99	0.29	33.70	0.53	33.76	0.38	34.57	0.26	34.02	0.42	33.35	0.56
TiO_2	0.51	0.11	0.29	0.12	0.33	0.17	0.24	0.10	0.45	0.14	0.42	0.16	0.40	0.27	0.56	0.20	0.39	0.21
Al_2O_3	33.56	0.65	34.47	0.73	33.44	0.72	33.63	1.21	34.84	1.20	34.16	1.06	35.26	0.78	34.72	0.77	35.29	1.38
FeO	14.77	0.47	15.21	0.58	15.61	0.77	16.48	0.87	13.91	0.43	14.81	0.79	11.70	1.49	11.41	0.72	12.52	1.71
MgO	1.25	0.12	0.56	0.15	0.65	0.23	0.25	0.14	1.22	0.31	1.09	0.36	2.46	1.08	2.75	0.36	1.45	1.03
CaO	0.17	0.06	0.19	0.08	0.19	0.09	0.07	0.02	0.21	0.06	0.18	0.05	0.20	0.11	0.26	0.09	0.13	0.08
MnO	0.16	0.03	0.14	0.06	0.08	0.03	0.10	0.02	0.14	0.05	0.11	0.03	0.09	0.02	0.09	0.02	0.33	0.53
Na_2O	1.99	0.13	1.90	0.15	1.88	0.15	1.91	0.25	1.90	0.11	1.86	0.18	1.72	0.27	1.78	0.12	1.69	0.17
K_2O	0.05	0.02	0.05	0.02	0.04	0.02	0.04	0.01	0.05	0.02	0.04	0.01	0.04	0.01	0.05	0.02	0.03	0.02
F	1.05	0.16	0.97	0.18	0.84	0.21	0.75	0.30	0.99	0.16	1.05	0.19	0.59	0.17	0.53	0.18	0.68	0.15
*H_2O	2.99	0.09	3.04	0.09	3.07	0.12	3.17	0.17	3.09	0.09	3.04	0.11	3.33	0.09	3.32	0.10	3.21	0.09
*B_2O_3	10.13	0.06	10.13	0.07	10.06	0.08	10.21	0.11	10.31	0.07	10.26	0.09	10.46	0.07	10.36	0.08	10.24	0.08
Total	99.71	0.45	99.82	0.56	99.24	0.45	100.83	0.50	100.80	0.53	100.77	0.49	100.81	0.38	99.84	0.72	99.32	0.47
Si (T) §apfu	5.68	0.05	5.64	0.07	5.71	0.05	5.78	0.03	5.68	0.09	5.72	0.05	5.74	0.04	5.71	0.04	5.66	0.09
Al (T)	0.32	0.05	0.36	0.07	0.29	0.05	0.22	0.03	0.32	0.09	0.28	0.05	0.26	0.04	0.29	0.04	0.34	0.09
Al (Z)	6.00	0.00	6.00	0.00	6.00	0.00	6.00	0.00	6.00	0.00	6.00	0.00	6.00	0.00	6.00	0.00	6.00	0.00
Al (Y)	0.46	0.10	0.60	0.10	0.51	0.11	0.53	0.16	0.60	0.14	0.54	0.14	0.64	0.15	0.58	0.12	0.72	0.18
Ti (Y)	0.07	0.01	0.04	0.02	0.04	0.02	0.03	0.01	0.06	0.02	0.05	0.02	0.05	0.03	0.07	0.03	0.05	0.03
Mg (Y)	0.32	0.03	0.14	0.04	0.17	0.06	0.06	0.04	0.31	0.08	0.28	0.09	0.61	0.27	0.69	0.09	0.37	0.26
Mn (Y)	0.02	0.00	0.02	0.01	0.01	0.00	0.01	0.00	0.02	0.01	0.02	0.00	0.01	0.00	0.01	0.00	0.05	0.08
Fe (Y)	2.12	0.08	2.18	0.09	2.26	0.13	2.35	0.15	1.96	0.07	2.10	0.13	1.63	0.22	1.60	0.10	1.78	0.25
Ca (X)	0.03	0.01	0.04	0.01	0.03	0.02	0.01	0.00	0.04	0.01	0.03	0.01	0.04	0.02	0.05	0.02	0.02	0.01
Na (X)	0.66	0.04	0.63	0.05	0.63	0.05	0.63	0.09	0.62	0.04	0.61	0.06	0.55	0.09	0.58	0.04	0.56	0.06
K (X)	0.01	0.00	0.01	0.01	0.01	0.00	0.01	0.00	0.01	0.00	0.01	0.00	0.01	0.00	0.01	0.00	0.01	0.00
vac.(X)	0.29	0.05	0.32	0.06	0.32	0.07	0.35	0.09	0.33	0.04	0.35	0.07	0.40	0.10	0.37	0.06	0.41	0.07
F (W)	0.57	0.09	0.53	0.10	0.46	0.12	0.41	0.16	0.53	0.09	0.56	0.11	0.31	0.09	0.28	0.10	0.37	0.08
OH	3.43	0.09	3.47	0.10	3.54	0.12	3.59	0.16	3.47	0.09	3.44	0.11	3.69	0.09	3.72	0.10	3.63	0.08
B	3.00	0.00	3.00	0.00	3.00	0.00	3.00	0.00	3.00	0.00	3.00	0.00	3.00	0.00	3.00	0.00	3.00	0.00

* H_2O and * B_2O_3 calculated by stoichiometry; §apfu, tourmaline structure formulae calculations based on 31 anions including 15 cations at T, Z, and Y sites (Henry and Dutrow, 1996). Abbreviations: Av. = average, SD = standard deviation.

TABLE 4. Average mole fractions of end-member components for tourmalines from the Heemskirk and Pieman Heads granites

Location	Feature	Schorl	Dravite	Tsilaisite	Uvite	Fe-Uvite	Foitite	Mg-Foitite	Olenite
Trial Harbor Heemskirk	Patch	0.53	0.08	0.01	0.00	0.03	0.26	0.04	0.06
	Orbicule	0.50	0.03	0.01	0.00	0.03	0.30	0.02	0.10
	Cavity	0.53	0.04	0.00	0.00	0.03	0.30	0.02	0.07
	Vein	0.55	0.01	0.00	0.00	0.01	0.34	0.01	0.07
	Mean	0.51	0.04	0.01	0.00	0.03	0.30	0.02	0.08
Granville Harbor Heemskirk	Orbicule	0.45	0.07	0.01	0.01	0.03	0.29	0.04	0.11
	Cavity	0.48	0.06	0.01	0.00	0.03	0.31	0.04	0.07
	Mean	0.46	0.06	0.01	0.00	0.03	0.31	0.04	0.09
Pieman Heads Granite	Patch	0.34	0.12	0.00	0.01	0.03	0.29	0.11	0.10
	Orbicule	0.35	0.14	0.00	0.01	0.03	0.26	0.11	0.09
	Vein	0.36	0.07	0.02	0.00	0.02	0.34	0.07	0.12
	Mean	0.35	0.09	0.01	0.01	0.02	0.32	0.08	0.11

TABLE 5. Summary of trace element compositions of tourmalines from the Heemskirk and Pieman Heads granites, analyzed by LA-ICP-MS

	Heemskirk Batholith			Heemskirk Batholith			Pieman Heads Granite (n=50)		
	Trial Harbor (n=63)			Granville Harbor (n=19)					
Elements	Range	Median	% bdl	Range	Median	% bdl	Range	Median	% bdl
Li	22.82 - 262.3	119.8	0	74.64 - 154.3	131.4	0	18.80 - 968.4	79.83	0
Be	1.79 - 64.51	9.36	2	3.46 - 62.09	9.71	0	0.89 - 22.32	3.69	24
P	40.69 - 512.1	81.49	25	41.37 - 284.7	73.11	26	48.15 - 189.1	81.59	22
Sc	1.22 - 118.6	45.61	0	5.10 - 83.10	23.63	0	0.84 - 109.9	49.92	0
V	0.49 - 62.97	10.73	3	2.42 - 78.04	32.49	0	0.24 - 180.6	60.51	4
Cr	0.23 - 19.29	7.9	60	2.59 - 74.28	20.75	5	1.05 - 40.65	6.4	60
Co	1.35 - 14.73	10.05	0	10.11 - 22.39	20.33	0	2.21 - 31.33	26.61	0
Ni	0.23 - 6.54	1.41	33	2.01 - 9.69	6.08	5	0.28 - 14.86	10.1	20
Cu	0.84 - 10.31	2.44	59	1.23 - 9.86	2.02	58	0.71 - 8.80	1.55	82
Zn	61.57 - 260.2	208.1	0	189.5 - 271.8	211.0	0	166.6 - 430.0	206.9	0
Ga	46.34 - 282.6	187.9	0	138.5 - 219.0	181.3	0	69.20 - 792.8	136.3	0
As	0.30 - 10.59	2.47	56	0.30 - 1.22	0.65	68	0.34 - 3.03	0.82	76
Rb	0.04 - 13.64	0.5	51	0.08 - 0.37	0.12	68	0.10 - 0.72	0.13	86
Sr	0.06 - 9.12	1.2	0	1.47 - 6.03	3.92	0	0.15 - 18.20	5.57	2
Y	0.01 - 8.77	0.08	27	0.02 - 0.14	0.05	47	0.01 - 0.54	0.06	42
Zr	0.12 - 6.64	0.39	5	0.03 - 1.51	0.33	21	0.02 - 3.46	0.28	24
Nb	0.86 - 70.38	5.67	0	1.17 - 27.52	1.82	0	0.20 - 5.16	1.6	0
^{95}Mo	0.08 - 1.71	0.42	57	0.09	0.09	95	0.07 - 0.44	0.16	90
^{98}Mo	0.06 - 1.34	0.32	54	0.04 - 0.12	0.08	89	0.09 - 0.31	0.24	92
Ag	0.06 - 0.09	0.07	87	0.08	0.08	95	0.03 - 0.06	0.05	96
Cd	0.21 - 4.60	0.44	87	0.19 - 0.30	0.25	89	0.13 - 0.45	0.19	86
Sn	19.33 - 289.2	44.8	0	3.42 - 35.29	4.97	0	3.50 - 98.18	13.65	0
Sb	0.10 - 1.09	0.17	81	0.19	0.19	95	0.07 - 0.19	0.16	92
Cs	0.01 - 19.38	0.16	37	0.02 - 0.26	0.05	53	0.01 - 0.69	0.11	64
Ba	0.04 - 0.80	0.1	56	0.09 - 0.24	0.13	63	0.05 - 0.75	0.16	52
La	0.13 - 11.60	2.34	0	0.48 - 3.39	2.12	0	0.04 - 6.48	0.93	6
Ce	0.29 - 25.35	4.2	0	0.87 - 6.23	3.98	0	0.07 - 8.83	1.68	6
Pr	0.03 - 3.36	0.39	3	0.08 - 0.59	0.32	0	0.01 - 0.78	0.17	16
Nd	0.13 - 9.78	1.23	10	0.19 - 1.52	0.79	0	0.03 - 1.97	0.52	28
Sm	0.03 - 4.52	0.33	30	0.05 - 0.39	0.14	26	0.03 - 0.28	0.1	56
Eu	0.01 - 0.10	0.03	57	0.02 - 0.14	0.07	32	0.01 - 0.25	0.09	48
Gd	0.03 - 1.79	0.21	37	0.03 - 0.20	0.1	53	0.02 - 0.25	0.06	58
Dy	0.01 - 0.75	0.09	52	0.01 - 0.10	0.03	58	0.01 - 0.16	0.05	64
Er	0.01 - 2.14	0.03	56	0.01 - 0.04	0.02	68	0.01 - 0.11	0.02	68
Yb	0.02 - 9.49	0.05	54	0.02 - 0.10	0.05	58	0.02 - 0.08	0.03	70
Hf	0.04 - 1.78	0.21	33	0.01 - 0.59	0.13	53	0.01 - 0.79	0.09	42
Ta	0.51 - 40.21	4.55	0	0.63 - 30.83	0.85	0	0.45 - 7.01	1.52	0
W	0.01 - 6.77	0.28	35	0.06 - 0.38	0.15	58	0.04 - 14.07	0.17	56
Au	0.03 - 29.48	0.1	63	0.10 - 1.11	0.23	79	0.02 - 18.70	0.14	76
Tl	0.01 - 0.15	0.03	75	0.01 - 0.03	0.02	79	0.01 - 0.05	0.02	86
Pb	0.17 - 3.82	1.1	0	0.67 - 2.22	1.21	0	0.06 - 15.25	1.96	0
Bi	0.01 - 0.66	0.08	37	0.01 - 2.25	0.12	32	0.03 - 14.26	0.3	38
Th	0.01 - 22.43	0.13	6	0.01 - 2.85	0.12	26	~0.01 - 2.49	0.03	32
U	0.01 - 4.22	0.08	38	0.01 - 3.44	0.02	53	~0.01 - 0.16	0.02	46